FINAL TECHNICAL REPORT

Reporting period: October 1, 2018—December 29, 2021

Capillary-driven Condensation for Heat Transfer Enhancement in Steam Power Plants

December 29, 2021

SUBMITTED UNDER AWARD NUMBER: DE-FE0031677

SUBMITTED BY: MIT

77 Massachusetts Ave. 3-461B

Cambridge, MA 02139

PRINCIPAL INVESTIGATOR

Evelyn N. Wang

Phone: 617-324-3311

Fax: 617-258-9346

enwang@mit.edu

TEAM MEMBERS

Yajing Zhao

yjzhao@mit.edu

Samuel Cruz

sacruz@mit.edu

SUBMITTED TO

U.S. Department of Energy

National Energy Technology Laboratory

CONTENTS

DISCLAIMER 4
ACKNOWLEDGEMENTS 5
LIST OF FIGURES 6
LIST OF TABLES 7
EXECUTIVE SUMMARY 8
ABSTRACT 10
INTRODUCTION 10
PROOF OF CONCEPT UTILIZING MICROMACHINNING ON SILICON with HIGHLY DEFINED GEOMETRY STRUCTURES 13
Modeling and Design of Structures 13
Vapor transport in membrane pores 13
COMSOL Multiphysics heat transfer coefficient model 21
Fabrication of Structures 29
Fabrication process flow 29
Fabrication of sample at large scale 30
Selectively Coating the Top Surface of Our Sample 32
Condensation in Ambient Air—Successful Proof-of-Concept and Elucidation of Physics 35
Heat Transfer Measurements in a Pure Vapor Ambient of Selectively-Coated Sample 39
SCALABLE METHODS FOR CAPILLARY-DRIVEN CONDENSATION 43
Materials Selection 44
Materials search for hydrophobic membrane 44
Materials search for porous metal wick 46
Proof of Concept based on Commercially Available Materials 49
Sample fabrication via diffusion bonding 50
Coating method 53
Micro-channels for condensate exit 54
Heat and mass transfer model 55
Condensation heat transfer experiment 57
Fabrication of Hydrophobic Membrane in a Scalable Way 62
Electrospinning PVDF-HFP membrane 62

Characterization of membrane properties 63
Factional factorial design for parametric optimization of electrospun membranes 66
Fabrication of Porous Metal Wick in a Scalable Way 68
Heat Transfer Prediction for Membrane-Covered Porous Copper Wick 69
REFERENCES 72

DISCLAIMER

ACKNOWLEDGEMENTS

This material is based upon work supported by the National Energy Technology Laboratory (NETL) of the U.S. Department of Energy with Richard Dunst as project manager under award No. DE-FE0031677.

LIST OF FIGURES

Figure 1. Steam condensation 11
Figure 2. Schematic of the novel capillary-driven condensation mode 12
Figure 3. Membrane pore mean permeabilities as a function pore diameter 15
Figure 4. Mean permeability of membrane as a function of pore diameter. 16
Figure 5. Micro-pillar unit cell. 22
Figure 6. Effect of wick size on the heat transfer coefficient 24
Figure 7. Effect of membrane pore diameter on the heat transfer coefficient. 25
Figure 8. Effect of membrane thickness on heat transfer coefficient. 27
Figure 9. Effect of the wicking length 28
Figure 10. Fabrication of high performance capillary driven condensation structure. 29
Figure 11. A 6" double side polished <100> silicon wafer 30
Figure 12. Successful large-scale fabrication of sample 31
Figure 13. Photoresist-wicking approach to selectively coat our sample 34
Figure 14. Experimental setup to observe horizontal condensation 36
Figure 15. Schematic of coated structure and condensation visualization study. 37
Figure 16. Visualization study of condensation in ambient air 39
Figure 17. Images showing the experimental configuration for the acquired data. 40
Figure 18. Bar plots of the heat flux (a) and heat transfer coefficient (b). 41
Figure 20. Images showing how the exit port works in our context. 42
Figure 21. Schematic of a capillary-driven condenser tube 43
Figure 22. Comparison of effective thermal conductivities 48
Figure 23. 3-dimensionally interconnected spherical pore network 49
Figure 24. Diffusion bonding assembly and the high temperature furnace 50
Figure 25. SEM images of the 3 hierarchical copper surfaces 51
Figure 26. Permeability characterization of the wick layer 52
Figure 27. Vapor deposition of FAS on porous copper sample. 53
Figure 28. Image (a) and schematic (b) showing a copper foam sample machined 55
Figure 29. Heat transfer enhancement given by the three hierarchical copper surfaces 56
Figure 30. Images taken inside (a) and outside (b-c) the environmental chamber. 58
Figure 31. (a) Filmwise condensation on a flat copper sample 58
Figure 32. Condensation experiments on fully hydrophobic hierarchical copper 59
Figure 33. Condensation experiments on biphilic hierarchical copper sample 60
Figure 34. Condensation experiments on biphilic, micro-channeled hierarchical copper. 61
Figure 35. Customized electrospinning setup for fabricating hydrophobic membranes. 62
Figure 36. SEM images of electrospun membrane samples 63
Figure 37. Wet curve and dry curve of an electrospun membrane sample 65
Figure 37. Pore size distribution of an electrospun membrane sample 65
Figure 38. An example of the reduced number of combinations 66
Figure 40. Results obtained from the screening study 68

Figure 41. SEM images of sintered copper powders 71

LIST OF TABLES

Table 1. Review of some key variables in model along with their units. 19
Table 2. Examples for commercially available hydrophobic membranes. 44
Table 3. Examples for commercially available porous metals. 47
Table 4. Properties of the copper meshes and copper foams. 50
Table 5. Fractional Factorial Design (FFD) for screening. 67

EXECUTIVE SUMMARY

Enhancing condensation heat transfer has important implications to reduce local water consumption, reduce CO_2 emissions, while simultaneously enhancing the overall cycle efficiency of steam power plants. This is important since most of the electricity produced in the U.S. comes from steam power plants. The state-of-the-art technology, dropwise condensation (DWC), has demonstrated its ability to achieve condensation heat transfer enhancements of up to an order of magnitude. However, it comes short of industrial implementation due to the requirement for thin coatings, which cannot adhere to the necessary industrial timescales required for operation. Therefore, various condensation approaches have been investigated to enhance the durability of condensation enhancing engineered surfaces.

Here we propose a novel condensation method which has the potential to address the concerns of durability by combining thick porous hydrophobic membranes with porous wicking structures on condenser tubes. This concept, termed capillary-driven condensation (CDC), can enhance condensation heat transfer to a level comparable to dropwise condensation according to our preliminary models. In this report, we explain this novel concept in depth, and investigate the physics during condensation on the CDC surfaces to understand, design, and develop superior condensation surfaces. We undertake two parallel approaches toward developing our surface.

In the first section of the report, we delve into a more fundamental understanding of the physics behavior of the proposed surface during condensation by fabricating a CDC sample on silicon with highly-defined geometry. We show the modeling, optimization, and rational design of a proposed surface, fabrication of that surface, visualization studies to elucidate the physics, and conduct experimental heat transfer measurements. We demonstrated our first successful proof-of-concept during vapor condensation. A non-optimized fabricated structure achieved a heat transfer coefficient ~ 240% higher than the theoretical filmwise value at the same operating condition.

Next, we explored the concept using scalable materials and approaches. We fabricated hierarchical copper surfaces with commercially available copper-based foams and meshes, and hydrophobized the copper mesh layer to realize capillary-driven condensation. We observed capillary-driven condensation on these hierarchical copper surfaces, and measured a 50% heat transfer enhancement over filmwise condensation on a micro-channeled, biphilic, hierarchical copper sample. Our model predicts a much higher heat transfer enhancement and we discussed the reason

for the discrepancy between the modeling results and the experimental measurements and the future work to further improve the condensation heat transfer on these hierarchical copper surfaces.

Finally, we explored scalable fabrication of the hydrophobic membrane and the porous metal wick. A parametric study has been conducted to optimize the fabrication recipe of the electrospun fibrous membrane. Sintering and electrodeposition have been studied for fabricating porous copper wick. Our heat and mass transfer model predicts > 5x heat transfer enhancement over filmwise condensation on an electrospun fiber covered sintered copper powder surface. Future work entails the realization of a scalable capillary condenser tube and experimental demonstration of its heat transfer enhancement.

Our main contributions are highlighted below:

1. Developed a novel silicon-based fabrication method to achieve our designed structures which are of fundamental interest and have potential applications in silicon-based electronics cooling
2. Developed physics-based analytical and finite-element models to design our surfaces and optimize for heat transfer performance
3. Provided in depth understanding of the physics of our CDC surfaces
4. Demonstrated a proof-of-concept on silicon and elucidated the physics of CDC surfaces
5. Demonstrated proof-of-concept on scalable surfaces made of commercially available materials
6. Conducted a parametric study on the fabrication of intrinsically hydrophobic membrane in a scalable manner
7. Investigated fabrication of porous wicking structures in large scale
8. Developed model framework to guide the design of a scalable CDC surfaces
9. Experimentally measured heat transfer enhancement on the scalable CDC surfaces

We recommend the following future work to achieve such surfaces industrially:

1. Explore scalable methods to fabricate micro-scale, high-thermal-conductivity, high-porosity wicking structures on the outer surface of round condenser tubes
2. Explore methods to attach thin, porous, hydrophobic membranes on the surfaces of tubes coated with thin wicking structures
3. Measure the heat transfer of tube-based CDC structures

ABSTRACT

A novel condensation method was developed to enhance the efficiency of steam power plants. The method consists of a hierarchical structure on the surface of condenser tubes consisting of a wicking structure overlaid with a porous hydrophobic membrane. The project is divided into two main efforts. First, a structure with highly defined geometry was made utilizing microfabrication on silicon. This structure helped us elucidate the physics of steam condensation at the surface, more easily model the heat transfer coefficient, and demonstrate the first proof-of-concept for our proposed condensation approach. The structures on silicon achieved a heat transfer coefficient ~ 240% higher than the theoretical filmwise value at the same operating condition. Second, the method is explored for scalability by fabricating surfaces with industrial class materials followed by heat transfer measurements on flat surfaces. An HTC enhancement of 50% over the experimental filmwise value was achieved on hierarchical copper surfaces made of commercially available copper foams and meshes, showing the potential of achieving heat transfer enhancement using low cost and scalable materials. Scalable fabrication of the hydrophobic membrane and the porous copper wick were also investigated. Our heat and mass transfer model predicts a > 5x heat transfer enhancement on a scalable version of capillary driven condenser made of membrane covered porous copper. The results demonstrate the promise of capillary-driven condensation surfaces for heat transfer applications.

INTRODUCTION

Thermoelectric power generators, which typically use a Rankine cycle, provide the majority of the electricity produced in the US[1]. However, they also withdraw the largest amount of water from US water bodies to condense the steam generated from the power plant. There is significant interest in enhancing the efficiency of condenser designs, which will not only improve power production but also decrease the amount for water needed for condensation. Significant efforts have focused on advancing condenser designs with higher performance for steam power plants. Various condenser designs have been proposed and incorporated in existing power plants[2]. These condensers, however, typically rely on filmwise condensation (Figure 1a), where a thin liquid film

on the condenser surface forms due to the high surface energy associated with the majority of industrial heat exchanger materials.

Filmwise condensation is not desired due to the large thermal resistance to heat transfer[3]. Over the past eight decades, dropwise condensation[4–9], where droplets roll off at sizes approaching the capillary length and clear the surface for re-nucleation (Figure 1b), has been researched and promises heat transfer enhancements of 5-10x compared to the filmwise mode.[10] Despite extensive development, maintaining robust non-wetting behavior has been an ongoing challenge and has prevented steam power plants from taking advantage of the heat transfer enhancement that dropwise condensation offers. The present work shows progress made toward the proposed new approach termed capillary-driven condensation (CDC). In this approach, a porous hydrophobic membrane atop a wicking structure on the condensing surface drives liquid transport and removal from the surface via a capillary pressure gradient along the wicking surface towards an exit port, as shown in Figure 2. This approach has a two-fold advantage. First, the structured wick increases the effective thermal conductivity of the condensate layer, reducing the thermal resistance. Second, the hydrophobic porous membrane helps generate additional capillary driving pressure to drive fluid out and significantly increase the heat transfer performance.

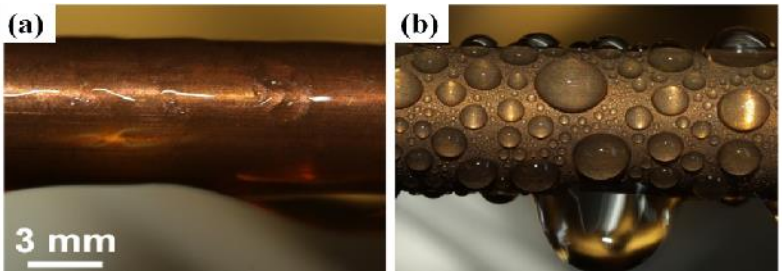

Figure 1. Steam condensation in (a) the filmwise mode on a bare copper condenser tube, and (b) dropwise condensation on a copper tube functionalized with a monolayer hydrophobic coating.

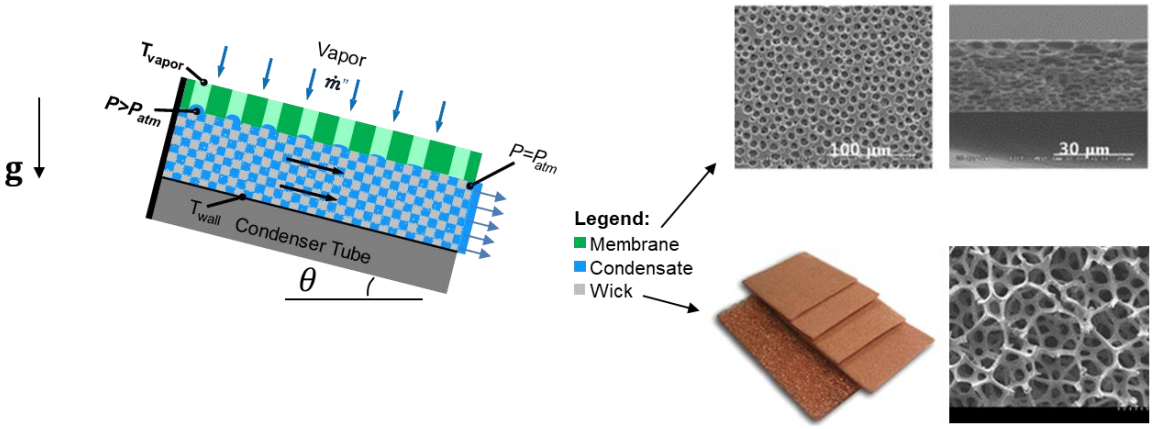

Figure 2. Schematic of the novel capillary-driven condensation mode on a wick structure covered by a porous membrane. The solid arrows within the wick indicate the condensate transport direction. Condensate transport is driven by the Laplace pressure from the outward-curving interfaces that form at the membrane during condensation and gravity depending on condenser orientation. An example porous membrane and structured wick are shown.

The major goal of this project aims to enhance the heat transfer coefficient of steam power plant condensers by the proposed new approach termed capillary-driven condensation (CDC). This goal is divided into smaller sub goals or objectives as follows. First, the structures composing CDC must be designed and developed. This includes designing a system composed of a hydrophobic membrane attached to a wicking structure where both are tailored to obtain optimal performance. Second, the structures are designed and subsequently fabricated followed by experimental demonstration. Third, the structure is optimized for maximum performance by further model development and experimental validation. Due to the nature of the work,

The scope of our work is to utilize analytical and finite element physics-based models to rationally design, optimize, and test our hierarchical engineered CDC surfaces to maximize heat transfer during condensation and demonstrate working proofs of concept utilizing highly-defined geometry on silicon microfabricated samples, and scalable industrial class metals and membranes. Our studies are limited to condensation being demonstrated on flat condensing surfaces. We provide recommendations for future work based on our results.

PROOF OF CONCEPT UTILIZING MICROMACHINNING ON SILICON WITH HIGHLY DEFINED GEOMETRY STRUCTURES

This section discusses the development and understanding of the proposed condensing surface. We elucidate the physics via modeling and experimentation utilizing rationally designed samples with highly-defined geometry. We discuss a preliminary analytical model, a heat transfer coefficient model, rational design selection utilizing our model, development of the fabrication, functionalization of our surfaces, visualization experiments, and heat transfer measurements.

Modeling and Design of Structures

Vapor transport in membrane pores

Our initial hypothesis was that there would be vapor transport in the membrane pores during operation of our CDC surface. We thus carefully develop a model considering vapor transport in membrane pores in this section. However, we later show that CDC operates better when the vapor transport resistance is minimized or eliminated, such as with thinner membranes or with liquid (rather than vapor) transport in the pores. Given that we expect fluid to condense inside of the wicking structure during the initial nucleation stage, vapor transport is expected to occur in the membrane pores. Furthermore, we can expect vapor transport when the meniscus of condensate is pinned at the bottom of the membrane pore at the wick-membrane interface. Therefore, it is important to understand and model the physics of vapor transport in our membrane. Nevertheless, we note that the type of transport in the pore is a function of the wettability of the membrane and its geometry. Here, we assume cylindrical geometry for the membrane pores as it simplifies the model. Moreover, we are able to make this geometry with our fabrication method. Therefore, we can both model and fabricate with the same geometry. The model is developed below along with discussion on the effect of saturated vapor operating conditions on the modelling approach.

To begin, the operating conditions of a power plant condenser, which are established by the saturation temperature and pressure of the steam, determine the type of flow that will occur through membrane pores. The vapor can flow in two major regimes. First, the vapor molecules can travel through a pore with minimal collisions between molecules, and most collisions with the membrane pore walls. This type of flow is termed free-molecule flow or Knudsen flow. In the other regime, molecule-molecule collisions dominate over wall-molecule collisions. This is called viscous flow, and the equations for this type of flow are well-developed. There is a regime called the transition

regime which considers molecule behaviour from both the Knudsen and the Poiseuille flow regime. To determine which regime we are in, the mean free path is compared against the pore diameter. The mean free path is the average distance that a molecule travels before it collides with another molecule. The mean-free path is given by the following relation

$$\lambda = \frac{k_B T}{\sqrt{2} P \pi d_c^2} \quad (1)$$

where k_B is the Boltzmann constant (1.3806485×10^{-23} J/K), T is the absolute temperature, P the average pressure within the membrane pores, and d_c is the collision diameter for water molecules (2.641×10^{-10} m). The ratio between the mean free path and the pore diameter is called the Knudsen number, and it gives a measure of the flow regime, $K_n = \lambda/d_p$. If $K_n > 10$ there is free-molecule or Knudsen flow. If $K_n < 0.01$, Poiseuille flow ensues. If we are in between, $0.01 < K_n < 10$, we are in the transition regime where descriptions from both types of flow should be included.

Many models have been developed to describe fluid flow through porous media. Among them is the well-known dusty-gas model. This model can capture free-molecule flow, viscous flow, and continuum diffusion as part of its development. Our system consists of a single, pure vapor of water molecules. Equations for this type of flow simplify significantly for this case.

In our analysis, we assume a steam saturation temperature of 35 ºC which is not uncommon near the condenser in steam power plants. The resultant mean free path is around 2.4 μm. Thus, different flow types can occur in membrane pores if the pore size is much larger, or much smaller, than 2.4 μm. In our analysis, we consider pore diameters up to 30 μm. For this operating condition, pore diameters below 250 nm can be said to be in the Knudsen flow regime and those above in the transition regime. For the transition regime, we must account for both the Knudsen and the Poiseuille flow contribution. Figure 3 shows plots of the mean permeability through a pore as a function of pore diameter for the case of pure steam. The operating saturation temperature of steam in power plant condensers can vary with outside-plant environmental conditions from about ~ 40° C to ~ 60º C.[12] Figure 3(a) shows a plot of the mean permeability as a function of pore diameter in the Knudsen regime, where the permeability is much smaller and only free-molecule flow is important. As can be seen, the permeability is much lower than the other two regimes. In contrast, Figure 3(c) shows the Poiseuille regime and much larger permeability values, which are desirable, but require larger pore diameters which are undesirable. Figure 3(b) shows the transition regime,

where it is necessary to account for both free-molecule and viscous effects through the pore. It is seen that the contribution of free-molecule flow becomes less significant for larger pore diameters, and eventually Poiseuille type flow dominates. Figure 4 shows a close-up of the transition regime for diameters from 0.1 – 15 μm, which is in our range of interest. It is seen that in this range, for the given operating condition, it is important to include the effects of both free-molecule and viscous flow. Neglecting the free-molecule flow contribution underestimates the vapor permeability by around a factor of ~2x. Thus, utilizing the Dusty-Gas model is appropriate versus utilizing Hagen-Poiseuille flow.

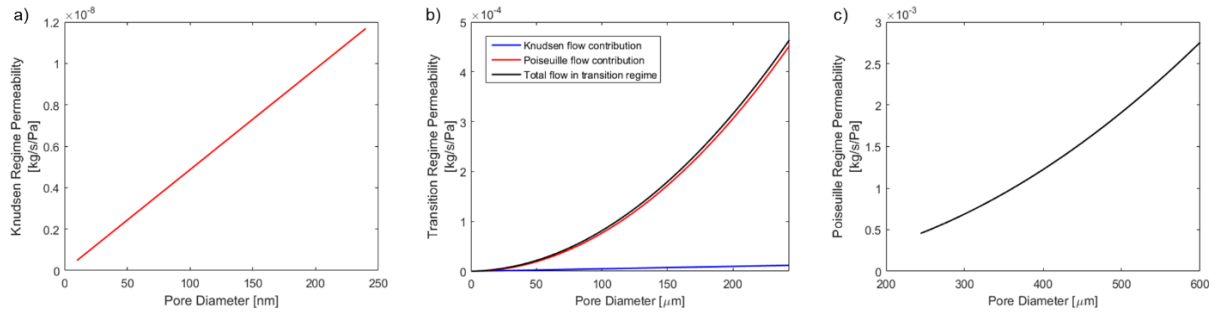

Figure 3. Membrane pore mean permeabilities as a function pore diameter in the three regimes. (a) the free-molecule flow or Knudsen regime, (b) the transition regime, and (c) the viscous flow or Poiseuille regime. The permeabilities in the Knudsen region are orders of magnitude lower than those in the transition and Poiseuille region. Thus, in that regime the driving force for condensation seen in the total temperature from membrane surface to condenser must be much larger to increase the flow. Alternatively, the transition regime is orders of magnitude higher. However, as the pore diameter increases the available maximum local capillary pressure decreases which is undesirable.

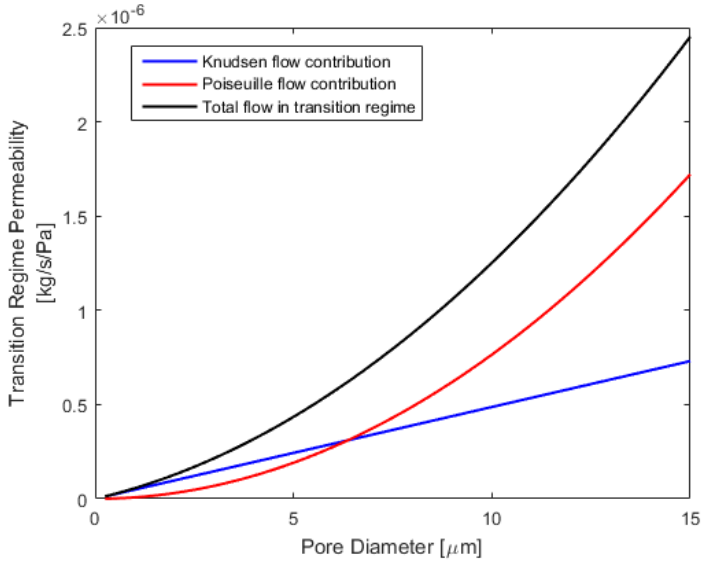

Figure 4. Mean permeability of membrane as a function of pore diameter from 0-15 µm in the transition regime for T_{sat} ~ 35°C. In this diameter range, there is a crossover point for each contribution at around 6 µm. Neglecting the Knudsen flow contribution by assuming purely viscous flow underestimates the permeability by almost ~2x.

When condensation occurs, a low-pressure region is created and flow is directed toward the condensing surface. The pure vapor pressure-driven flux in the transition region can be described by

$$J = \frac{\bar{K}}{RT}\frac{\Delta p}{t_m} \qquad (2)$$

where R is the gas constant (8.3144598 J/mol/K), T is the absolute temperature, Δp is the pressure drop across the membrane, t_m is the thickness of the membrane, and $\bar{K}$ is the mean flow permeability for a pure gas given by,

$$\bar{K} = D_{iK} + \frac{\bar{p}B_o}{\mu_{ii}} \qquad (3)$$

where D_{iK} is the Knudsen diffusion coefficient, $\bar{p}$ is the average pressure in the pore, B_o is the viscous flow parameter, and μ_{ii} is the viscosity coefficient for pure vapor. The Knudsen diffusion coefficient can be shown to be proportional to the mean molecular speed from the kinetic theory of gasses,

$$D_{iK} = \frac{4}{3} K_o \bar{v} \tag{4}$$

where K_o is the Knudsen flow parameter or permeability coefficient in free molecule or Knudsen flow regime, and $\bar{v}$ is the mean molecular speed and is given by,

$$\bar{v} = \left(\frac{8RT}{\pi M}\right)^{\frac{1}{2}} \tag{5}$$

It is worth noting the transport coefficients and proportionality constants depend on the structure of the porous medium. For the simple case of a porous membrane consisting of cylindrical pores of length t_m and diameter d_p the Knudsen and Poiseuille flow parameters are simply related as $K_o = d_p/4$ and $B_o = d_p^2/32$ respectively. Thus, the mean flow permeability becomes,

$$\overline{K} = \frac{1}{RT t_m}\left(\frac{1}{3} d_p \left(\frac{8RT}{\pi M}\right)^{\frac{1}{2}} + \bar{p}\frac{d_p^2}{32\mu_l}\right) \tag{6}$$

where t_m is the membrane thickness, R is the gas constant, T is the absolute temperature, $\bar{p}$ is the average pressure in the pore, M is the molar mass, μ_l is the liquid viscosity, and d_p is the pore diameter. The first term inside the brackets is the Knudsen mean permeability, which is directly proportional to the pore radius. The second term is the viscous or Poiseuille flow permeability, which is proportional to the pore diameter squared. As such, we can note that with increasing pore radius, the permeability increases faster in the Poiseuille regime than in the Knudsen regime. Equation 6 above is for the transition region, and through the dusty-gas model simple additivity of both effects is implemented to account for both, since the contribution for higher order non-linear logarithmic terms is assumed to be small. Usually, it is up to individual experiments to determine how good this approximation is, though previous work is stated to have shown excellent agreement. Critiques of this assumption can be found in reference[11]. In addition, the quantities inside the pore are approximated, such as the temperature and average pressure.

The flux through a pore can now be calculated by multiplying the mean permeability through a pore by the pressure across the membrane

$$J = \bar{K}\Delta p \quad (7)$$

$$\Delta p = (P_{vap} - P_{sat}(T_{wall} + \Delta T_{wick})) \quad (8)$$

where P_{vap} is the vapor pressure, and $P_{sat}(T_{wall} + \Delta T_{wick})$ is the liquid saturation pressure at the wick-membrane interface, here used as an approximation to the saturation pressure right outside the liquid-vapor interface at the bottom of the pore. The units of equation 6 are moles/m^2/s. To convert this to a mass flow rate, we multiply by the molar mass M in kg/mol. This quantity refers to the mass flux in the area of one pore, so we multiply by the total frontal surface area A_T and the membrane porosity ϕ_m to obtain the total mass flow rate through the membrane. The mass flow rate through the pore is then given by,

$$\dot{m}_c = \bar{K}\Delta p M A_T \phi_m \quad (9)$$

Assuming a square shape to the frontal condensing surface of length L, $A_T = L^2$, and if $L/4t_{wick} \gg 1$, or if the wick sides are covered by an impermeable material, then condensation on the sides of the wick can be neglected. Maximizing the membrane mass flux is crucial. Since the membrane determines both the maximum possible driving capillary pressure available, and the mass flow capacity through the frontal area, which are both limited by the pore diameter, optimizing the pore diameter and maximizing the porosity is crucial.

An enthalpy balance yields the following equation, accounting for condensation in each pore through the frontal surface area,

$$q'' A_T \phi_m = \dot{m}_c h_{fg} \quad (10)$$

Heat flux through the wick—assuming this is constant through the frontal area of the wick, which is not necessarily true since the membrane is on the frontal surface and the open pore area transfers heat by phase- change but the solid area is assumed to insulate—is given by

$$q'' \approx \frac{k_{eff}}{t_m}\Delta T_{wick} \quad (11)$$

Here, k_{eff} is the effective thermal conductivity of the wick, and ΔT_{wick} is the temperature drop across the wick. Finally, we describe flow through the structured wick by first utilizing Darcy's law,

$$q = -\frac{\kappa}{\mu_l}\left(\frac{dp}{dx} - \rho_l g\right) \quad (12)$$

where κ is the structured wick permeability, μ_l is the liquid dynamic viscosity, ρ_l is the liquid density, g the gravitational constant, and $\frac{dp}{dx}$ the additional driving pressure gradient from capillarity.

By adding a membrane atop the wicking structure, we are promoting additional fluid driving pressure by capillarity as well as a vapor transport resistance through the thickness of the membrane. With careful design of the membrane, we can find a trade-off where it may be optimized to maximize the additional capillary driving pressure, while minimizing resistance to flow. The additional capillary-driving pressure produced can be approximated by the following expression for cylindrical pores, which represents the maximum capillary pressure that can be sustained by a pinned meniscus, or the burst pressure to enter a pore,

$$P_{cap,\ max} = P_0 - P_L = \Delta P_{max} = \frac{4\sigma}{d_p}\cos(CA - 90) \quad (13)$$

where $P_{cap,max}$ is the pore-entry burst pressure, P_0 is the pressure of the vapor above the interface, P_L is the pressure of the liquid just below the interface, σ is the liquid surface tension, CA is the contact angle of the hydrophobic membrane, and d_p is the radius of curvature of the liquid-vapor interface emanating from the pore, assumed to be the pore diameter at the burst pressure. A review of key variables is shown below in Table 1.

Table 1. Review of some key variables in model along with their units.

Variables	Description	Units
J	Mass Flux	[moles/s/m^2]
$\overline{\mathrm{K}}$	Mean pore permeability	[moles/s/m^2/Pa]
Δp	Pressure drop across membrane	[Pa]
q''	Heat flux	[W/m^2]
t_{wick}	Wick thickness	[m]
t_m	Membrane thickness	[m]
d_p	Membrane pore diameter	[m]

k_{eff}	Structured wick effective thermal conductivity	[W/m/K]
κ	Structured wick intrinsic permeability	[m^2]

Equations 1 through 13 form a complete picture of our preliminary model which considers vapor flow in the transition regime. This model describes the expected behaviour from CDC surfaces when condensation happens with vapor transport in the pores. Despite of the type of transport in the pores, whether liquid or vapor, the transport in the wicking structure of the model continues to apply. To describe liquid transport in the pores, we simply consider the fluid mechanics in the pore coupled with the Schrage equation (or the moment-method) for condensation. The overall trends remain similar. We prescribe reasonable values for multiple variables in the model and sweep others to understand trade-offs in design and the expected heat transfer during condensation. Our goal was to obtain the maximum possible heat transfer performance while avoiding surface flooding, which degrades heat transfer. Based on preliminary modelling, we found that we require wicking structures with high permeability as well as effective thermal conductivity. However, it was found that thermal conductivity becomes less important for higher permeabilities. Thus, designing for higher permeabilities becomes a priority. The model highlights bounding values above which we should design. Moreover, to optimize heat transfer performance, pore diameters are below 20 μm. Smaller optimized pore diameters yield higher capillary pressure and heat transfer performance. Note that the hydrophobic membrane was here assumed to be a cylindrical through-pore membrane, but this geometry is not necessarily required for operation.

The preliminary model showed us that it was advantageous to design for a thin wicking structure with high thermal conductivity and high porosity, utilize the thinnest membrane possible with the smallest pores that could sustain the liquid thin film below designed level and avoid flooding at a given operating conditions. For brevity, those results are not presented here, but rather we present a finite element heat transfer coefficient model in the next section. This model is built utilizing geometry which is directly related to the structure we will fabricate, one characterized by highly-defined geometry.

COMSOL Multiphysics heat transfer coefficient model

The previous section introduced an analytical model which was helpful to get initial estimates of the characteristic length scales required for our hierarchical structured CDC surface and their expected performance. Moreover, that model revealed general trends on how such surfaces operate. We learned that the geometry of either the wick and the membrane determine the magnitude of their associated heat and mass transfer resistances, which can be independently designed and optimized to enhance heat transfer. In this section, we describe a model which is utilized to rationally design our CDC surfaces utilizing highly defined geometry. This will allow us to tailor our designs to attain the highest HTC possible at a given operating condition, while simultaneously avoiding top-surface flooding. We will later explain how flooding occurs on our surfaces in our visualization studies. COMSOL is utilized to calculate both the permeability and the heat transfer coefficient (HTC) for micro-pillared wicks as a function of the geometry of the hydrophobic membrane and the wick. Later versions of this model utilize analytical permeability results for micropillar wicks from Byon and Kim.[11] The results from the HTC model are combined with analytical porous media models, and mechanical stability calculations, to find the flooding criteria, and mechanically stable surfaces, respectively. From the results we were able to then select rational designs.

For the HTC, we utilize a conduction model neglecting convection effects due to a small Jakob and Peclet numbers in the condensate flow direction of the wick. The HTC is calculated on a micro-pillar unit cell (Figure 5) and later by a quarter-pillar unit cell described by the diameter d, pitch l, and the diameter to pitch ratio d/l, and the pillar height h, which is the wick thickness. We make the condensation heat flux at the surface of the unit cell a function of vapor transport through a cylindrical pore and scale this over the frontal condensation surface area using a prescribed membrane porosity. Other variations of the present model (not shown here for brevity) also calculate the HTC with the condensate meniscus pinned at the top of the membrane, and liquid transport in the pores.

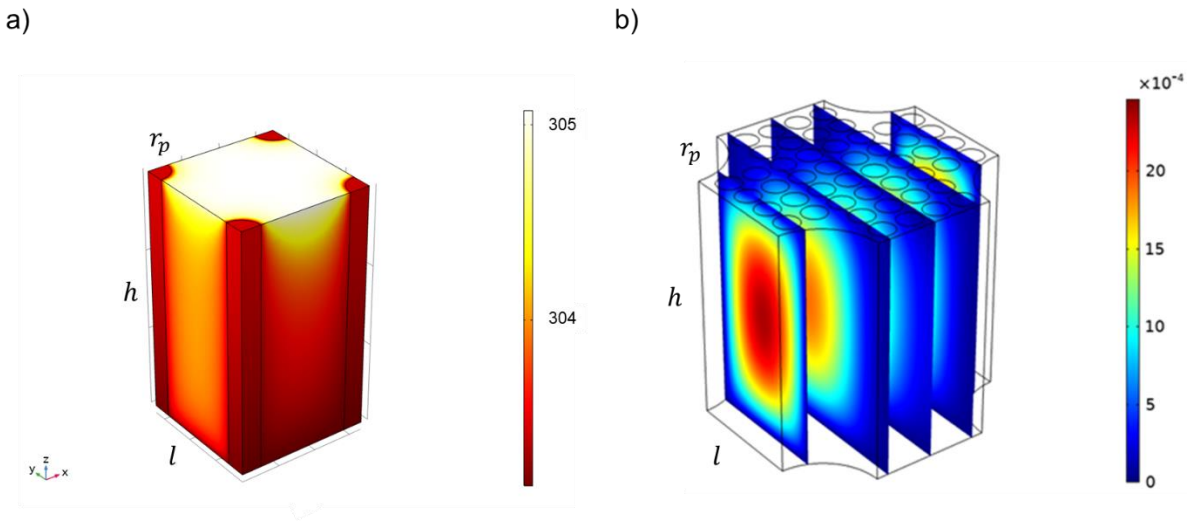

Figure 5. Micro-pillar unit cell utilized for (a) the HTC simulation, which includes solid pillars and (b) the permeability simulation, which contains the fluid body with no-slip condition at the wall boundaries. Half of the unit cell was used for the permeability calculation due to symmetry. A quarter of the unit cell shown in (a) is used for the HTC measurement due to symmetry (not shown).

For vapor transport through the membrane pores, we utilize the dusty-gas model from the previous section and update the previous equation. Previously, the equation was limited to large ratios of the thickness of the membrane t_m to the pore radius r_p (or very thick membranes). In this case, the transmission probability—the probability that a molecule entering the pore from the top surface will make it all the way across the membrane—simplified to $\eta \approx 2.67(r_p/t_m)$. However, as the membrane thickness decreases and the ratio is close to unity or a little less, this assumption is no longer valid. Thus, we modify the transmission probability after the equations provided by Berman.[12] First, a reduced length, $L = t_m/r_p$, is introduced for a cylindrical pore. Then, the transmission probability across the pore is approximated by equation 14 below. This equation is then utilized in the dusty-gas model for vapor transport in the transition regime.

$$\eta = 1 + \frac{L^2}{4} - \frac{L}{4}\sqrt{L^2+4} - \frac{\left((8-L^2)\sqrt{L^2+4}+L^3-16\right)^2}{72L\sqrt{L^2+4}-288\ln\left(L+\sqrt{L^2+4}\right)+288\ln 2} \qquad (14)$$

Next, we calculate the HTC, viscous pressure-drop across the structure for a given subcool, and estimate the stressed induced on the membrane to predict possible membrane failure. Figure 6 shows the effect of wick size on the HTC taking flooding into account. The wick sizes represented

include pillar wick diameters from 3 μm to 30 μm, and a sweep of d/l ratios from 0.05 to 0.98. The pillar height is 30 μm. Over this wide range, we note that in both designs the HTC is higher for smaller wick geometries. The HTC also varies as a function of d/l ratio. At low d/l ratios, the HTC is smaller due to a lower solid fraction. As the solid fraction increases, where $\phi_s = 0.25\pi(d/l)^2$, the HTC goes up until it reaches a maximum. At higher d/l ratios, the HTC begins to decrease due to less membrane area being available for condensation due to a larger wick solid fraction and the fact that pillar tops are insulated in the model as a conservative estimate (in practice, droplets can nucleate on the top surface of pillars). Moreover, each data point is checked for flooding. Flooding occurs when the viscous pressure drop in the wick exceeds the highest capillary pressure in pinned menisci on membrane pores. Flooded data points are plotted with black circle markers to show they are off limits. Flooded points occur at high solid fractions, where the permeability is low. Figure 6(a) represents a structure with a pore diameter of by 1 μm, and Figure 6(b) a structure with a pore diameter of 3 μm. The smaller pore diameter produces a larger capillary pressure to drive fluid through the wick. Notably, for the small pore diameter, more points are accessible along the curves before flooding occurs. However, the smaller pore diameter poses a larger vapor transport resistance, and thus the HTC is generally lower (compare the y-axis of (a) and (b). However, the combined effect is such that a similar performance is expected from both designs. As we will find later, we can operate in a regime where no vapor transport is expected, and in fact find that vapor transport in the ports is not an ideal configuration as droplet absorption is the mechanism by which the surface stays dry. Nevertheless, the present results are directly relevant to the case with no vapor transport, as the general trends are upheld and are shifted by a value. As we will see in the visualization experiments, it is possible to add to the model the heat transfer from droplets that grow on pillar tops and are absorbed with some frequency τ. Here, we take a conservative estimate and neglect this value, since we do not know the absorption frequency at the given operating configuration in a pure vapor environment. The results from Figure 6 show that multiple designs which can attain to our desired performance may be selected. Thus, a design with the simplest geometry among those with similar performance may ultimately be selected. The black dashed line in both plots represents the expected performance with dropwise condensation at the same vapor temperature and subcool calculated using a simple model by Rose.[13] The wall and vapor temperatures were chosen close to commercial operating conditions of condensers as 30°C and 32°C, respectively. Based on our initial model, this lower subcool is a reasonable value

to choose since our surfaces are expected to yield a lower the subcool at the same operating conditions than filmwise condensation. This value also allows us to determine the expected HTC for this particular operating configuration with vapor transport in the pores. Later we will see that this configuration—with vapor transport in the pores due to a completely hydrophobic membrane—actually yields many parasitic top-surface droplets. However, we conduct visualization studies to determine the physics and find a membrane configuration which avoids such droplets.

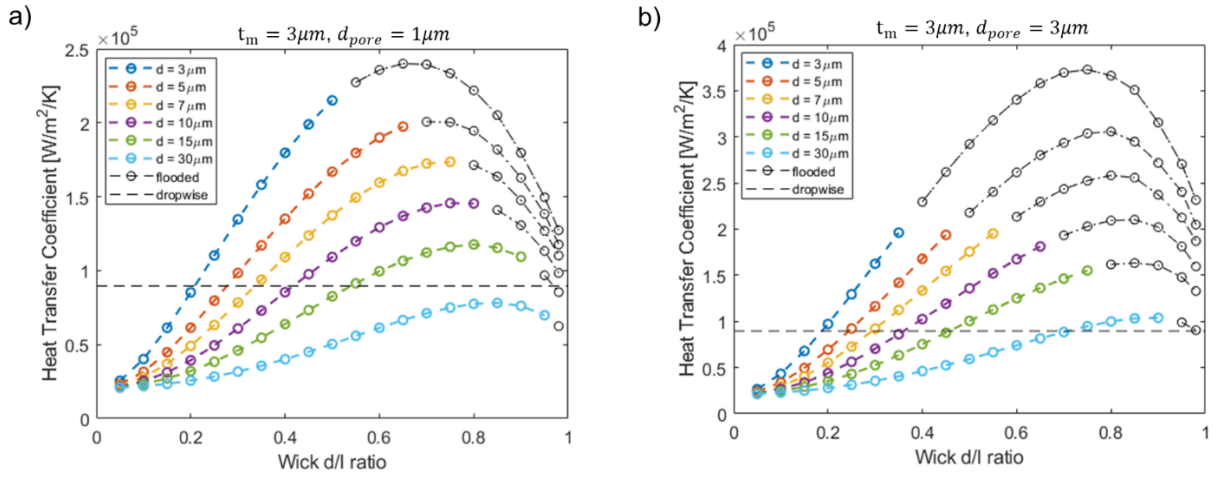

Figure 6. Effect of wick size on the heat transfer coefficient by varying the pillar wick diameter and the d/l ratio for a 3µm thick membrane with (a) 1µm pore diameter and (b) 3µm pore diameter. The pillar height is 30µm.

Figure 7 shows the effect of micro-pillar wick solid fraction and membrane pore diameter on the HTC. The general trend shows that larger pore diameters can produce larger HTC's due to reduced vapor transport and a higher heat flux at a fixed subcool. However, considering flooding, many of the points which produced enhancement became flooded at larger wick-solid fractions since the capillary pressure in larger pores could not sustain the viscous pressure drop across the wick (L_w = 1.27 cm). The net result is that larger pore diameters resulted in more flooded points, and the corresponding available designs for a given pore diameter were only accessible at smaller HTC enhancements. In contrast, smaller pores have less flooded points due to higher capillary driving pressures, and designs at higher wick-solid fractions—which have higher HTC's—are accessible. Our fabrication capabilities allow pore diameters no smaller than 1 µm in diameter, since this is the resolution limit of the UV and laser exposure tool in the photolithography step.

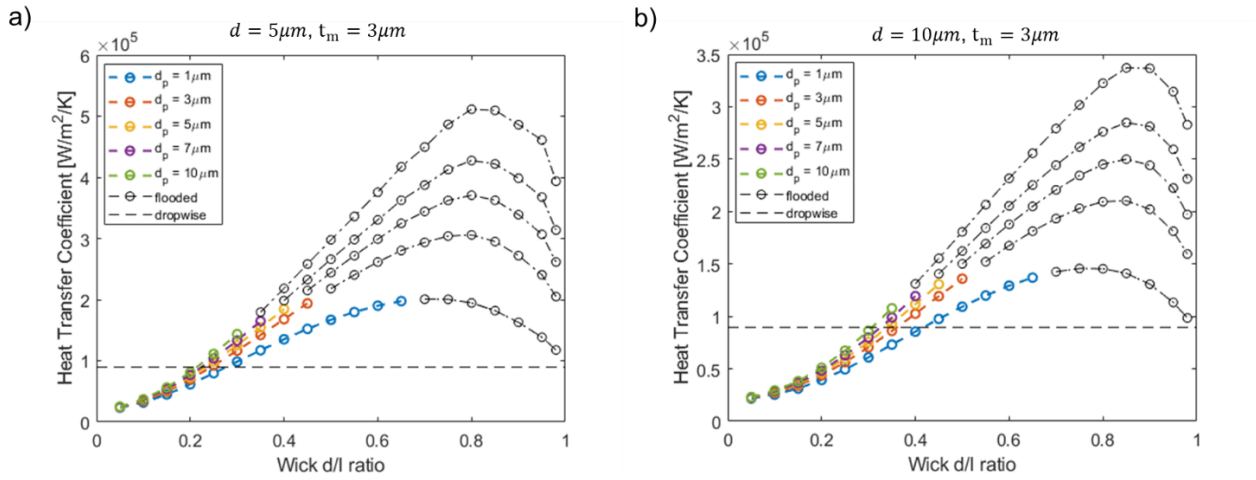

Figure 7. Effect of membrane pore diameter on the heat transfer coefficient for a membrane thickness of 3μm and two different wick sizes represented by pillar wick diameters of (a) 5 μm and (b) 10 μm. The pillar height is 30 μm.

Figure 8 shows the effect of membrane thickness on the HTC. Thinner membranes mean shorter pores and reduced vapor transport resistance, which results in higher possible HTC's. However, as the membrane gets thinner, it can become too weak to sustain the local capillary pressure generated in the pores of the membrane. Here, we consider the mechanical strength of the membrane. The membrane can be made from deposited materials such as SiO_2 or SiN_x on Si wafers. Tsuchiya, Inoue, and Sakata measured the tensile strength and fracture toughness of plasma enhanced chemical vapor deposited (PECVD) SiO_2 thin films.[14] For 650nm thick SiO_2 thin films, they found the mean tensile strength to be 1.2-1.9 GPa in vacuum and 0.6-1.0 GPa in air, while the mean fracture toughness is 1.3-2.0 MPa-$m^{1/2}$ in vacuum and 0.6-0.9 MPa-$m^{1/2}$ in air. Similarly, Yoshioka, Ando, Shikida and Sato measured the fracture strain and the Young's modulus of thermally oxidized SiO_2 on single crystal silicon and low-pressure chemical vapor deposited (LPCVD) Si_3N_4 thin films.[15] They measured Young's Moduli of 74 GPa and 370GPa and fracture strains of 2.5% and 3.8% for SiO_2 and Si_3N_4, respectively. We estimate the fracture strength from these values as $\sigma_f = E\epsilon_f$, where σ_f is the stress at fracture, E is the Young's Modulus, and ϵ_f is the strain at fracture. Thus, the stress at fracture for SiO_2 and Si_3N_4 can be estimated as 1.85 GPa and 14.1 GPa, respectively. As seen, the experimentally measured tensile strength values for these two materials vary significantly. In our fabrication, we utilize a low

pressure chemical vapor deposited (LPCVD) low-stress SiN_x thin-film (membrane) with a thickness of ~ 500 nm. We can set up a simple analytical model to compare the lower values of the tensile strength to an estimated bending stress assuming a rectangular beam geometry with the beam base representing the pillar diameter and the beam thickness the membrane thickness. Assuming a beam pinned at both ends, the maximum bending moment at the center of the beam is given by equation 15,

$$M_c = \frac{\sigma_L L^4}{384EI} \quad (15)$$

where σ_l is the distributed load, L is the longest length connecting two pillars in a unit cell, E is the Young's Modulus, and I is the moment of inertia. The moment of inertia for the assumed geometry is given by equation 16,

$$I = \frac{d t_m^3}{12} \quad (16)$$

where d is the pillar diameter representing the beam width, and t_m is the membrane thickness. The maximum bending stress at the center is then given by equation 17.

$$\sigma_b = \frac{M_c\left(\frac{L}{2}\right)}{I} \quad (17)$$

The distributed load is overestimated and assumed to be the highest local Laplace pressure generated in a superhydrophobic pore which is $4\sigma/d_p$. In reality, the pore is not superhydrophobic and this value is scaled down due to a lower contact angle. The smallest pore in this study (1 μm) yields a local pressure of 0.28 MPa for the overestimated value. From this load one can calculate the bending stress for different unit cell geometries and compare it to the available measurements of the tensile strength for the materials and geometries utilized. A quick calculation utilizing a wick geometry with $d = 7\mu m$, $d/l = 0.5$, and membrane made of Si_3N_4 with geometry with $d_p = 1\mu m$ and $t_m = 8\mu m$, reveals that the maximum bending stress is 3.79 GPa, which is close to the 14.1 GPa tensile strength estimated from reference.[15] Smaller thicknesses for the membrane utilizing this model yield higher bending stresses. However, values for the principal stresses which are representative of the geometry here modelled are required to obtain better estimates. We have thus computed finite element simulations of the first principle stress using the fabricated geometry with COMSOL Multiphysics. The results show that that the first principle stress is much lower (~10 x) than the expected tensile strength for a 500 nm membrane. Therefore, we expect our

membrane to uphold the required capillary pressures from the constrained fluid layer in the wick. Despite this result, each designed geometry should be checked for failure, especially as the membrane thickness decreases and the pillar pitch increases. Nevertheless, we have pinpointed the main failure mechanism. Notably, the largest bending moment varies as $\sim L^4$ which is a strong dependence on the pillar spacing. Thus, to reduce the bending stress and achieve thinner membranes, one needs to consider smaller pillar to pillar spacing.

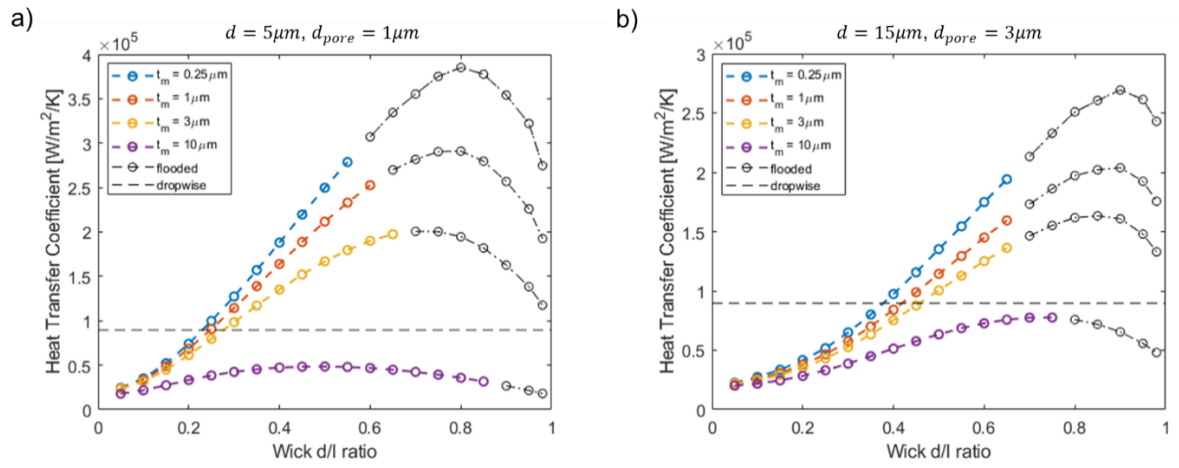

Figure 8. Effect of membrane thickness on heat transfer coefficient as the wick d/l ratio is varied for two different wick geometries (a) for a pillar wick diameter of 5 µm and a membrane pore size of 1 µm and (b) for a larger pillar wick diameter of 15 µm and a membrane pore size of 3 µm. The pillar height is 30 µm.

Figure 9 shows the effect of wicking length L on the HTC and available designs. For the same design, increasing the wicking length has the effect of reducing the number of available design geometries due to the increase of viscous pressure drop with length, which yields flooding of the structure. This means that the capillary pressure in the pore cannot sustain the viscous pressure drop, and liquid is ejected from the front surface of the membrane. One way to combat this is to utilize smaller pores. However, smaller geometries than the present utilized are significantly more challenging to fabricate. Notwithstanding, we can expect significant heat transfer enhancement utilizing the present geometries which are designed for wicking lengths on the order of half the circumference of ½" condenser tubes. Moreover, we recall that we can make thicker wicks to reduce the viscous pressure drop and maintain our membrane size, all while still maintaining HTC

enhancement. The exit port can also be engineered to reduce the wicking length and increase the HTC. Engineering the location and number of exit ports also allows us to introduce new design geometries not accessible. However, we limit the scope of this study to the exit port at the edges of our sample. We note that even for larger wicking lengths (Figure 9(b)), there are still available designs close to the level of dropwise condensation that will not flood. This means that significant heat transfer enhancement can still be achieved even with a wicking length of 1". As already mentioned, the wicking lengths modelled—1" and ½" inch—are industrially relevant length scales for condensers in steam power plants.

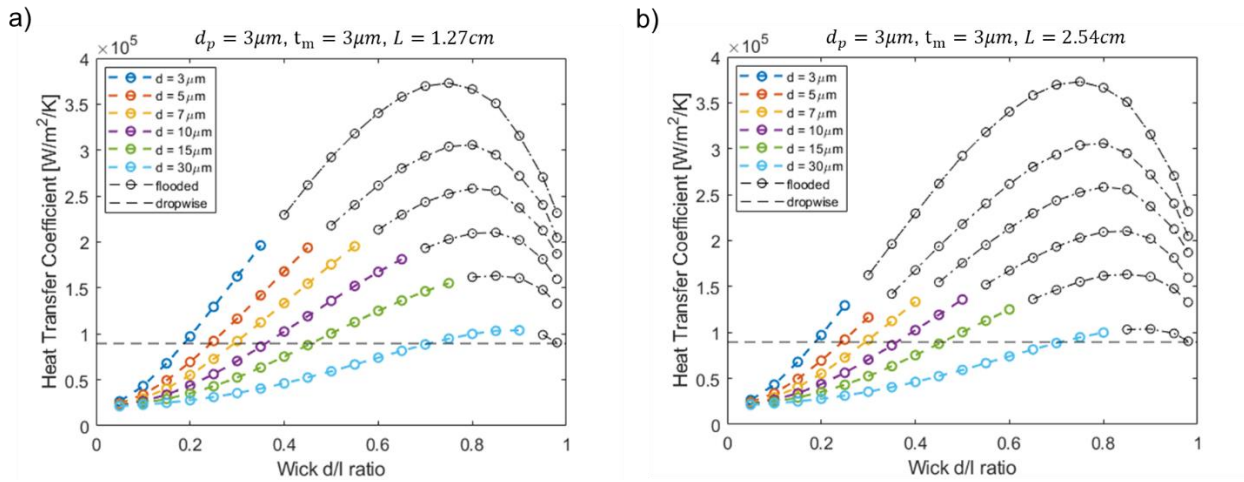

Figure 9. Effect of the wicking length on available designs and attainable heat transfer coefficients. Longer wicking lengths require higher capillary-driving pressures, so less designs are available due to flooding. The pillar height is 30 μm.

The modelling in this section helps us understand the relationship between the geometry in the wicking structure and that of the membrane. Specifically, the model shows how the geometries affect the HTC, flooding criteria, and mechanical stability of the membrane. The next section details the fabrication for the structures which were rationally selected utilizing a model with the framework shown in this section.

Fabrication of Structures

Fabrication process flow

The proposed fabrication for the capillary-driven condensation structure is shown in Figure 10.

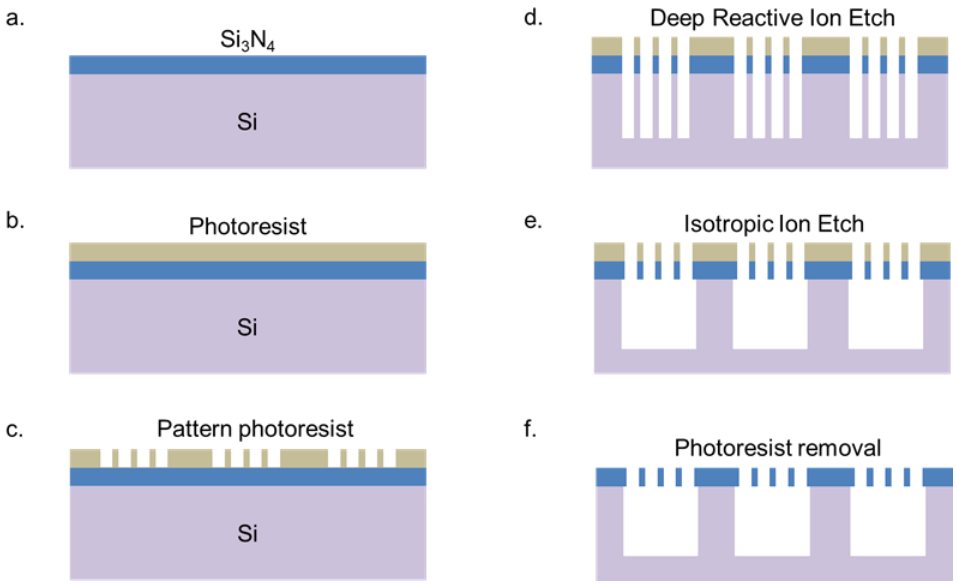

Figure 10. Fabrication of high performance capillary driven condensation structure.

We utilize a double-side polished silicon wafer (150 mm diameter, ~ 675 μm thick, <001> orientation) and coat a 500 nm layer of low-stress silicon nitride utilizing LPCVD (Figure 10(a)).

Next, we utilize photolithography to pattern a pillar-pore array on the silicon nitride coated side of the wafer (Figure 10(b) & (c)). In Figure 10(d), deep reactive ion etching (DRIE) is utilized to etch the pores in the nitride layer and form the foundation of the wicking structure. In Figure 10(e), an isotropic etch is utilized to remove excess silicon between the pore pattern in the silicon to create the micropillar wicking structure, while maintaining the pore geometry of the silicon nitride membrane. Finally, the remaining photoresist is removed utilizing plasma etching. A self-assembled monolayer (SAM) coating is then utilized to render the surface hydrophobic. We attempt various ways of coating the membrane and settle for a method detailed in a latter section. This condenser surface facilitated demonstration of our first successful proof-of-concept on silicon. Figure 11 shows a 6" wafer coated with ~ 500 nm of low stress silicon nitride which was utilized for one round of fabrication.

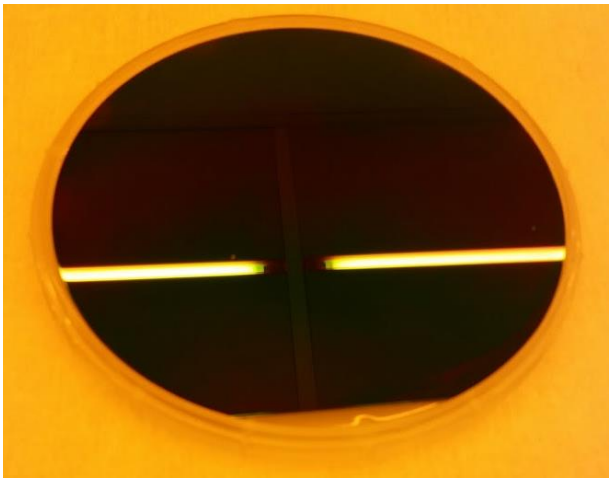

Figure 11. A 6" double side polished <100> silicon wafer is coated with 500 nm of low stress silicon nitride, as designed with our simulation

Fabrication of sample at large scale

We initially fabricated a millimetre scale sample in order to test the feasibility of the proposed fabrication approach. It was found that we were able to generally achieve the desired structure and thus showed the feasibility of our approach. We moved on to scaling up our design to the centimetre scale to demonstrate the fabrication at industrially relevant length scales. In this attempt, we found it difficult to achieve a large-scale printing of our pattern onto the photoresist utilizing direct-write lithography due to the large size of the drawing. We thus ordered our design in a photomask from a company and tried utilizing the UV light exposure tool. However, this approach did not yield good results due to spatial variations in the exposure dose at these critical dimensions (~ 1 μm feature size). In this section, we again utilize the MLA-150 direct write lithography tool, and utilize a feature workaround to print our large drawing successfully. Previously, we could not print large patterns due to the high density of the drawing caused by the many circles that needed to be converted into the format of the tool. However, we found a feature on the tool that could be used as a workaround. Briefly, a smaller millimetre-sized unit cell of the structure was copied in space and "stitched" together to achieve centimetre scale structures. Smaller drawings could successfully be converted to the tool's format, whereas larger drawings could not. Thus, we utilize a pattern "stitching" approach to fabricate our centimetre-scale sample. Fabricating one design at a time then became a feasible approach rather than printing multiple

designs on large areas of a 6-inch wafer using either direct-write lithography or a photomask with UV exposure.

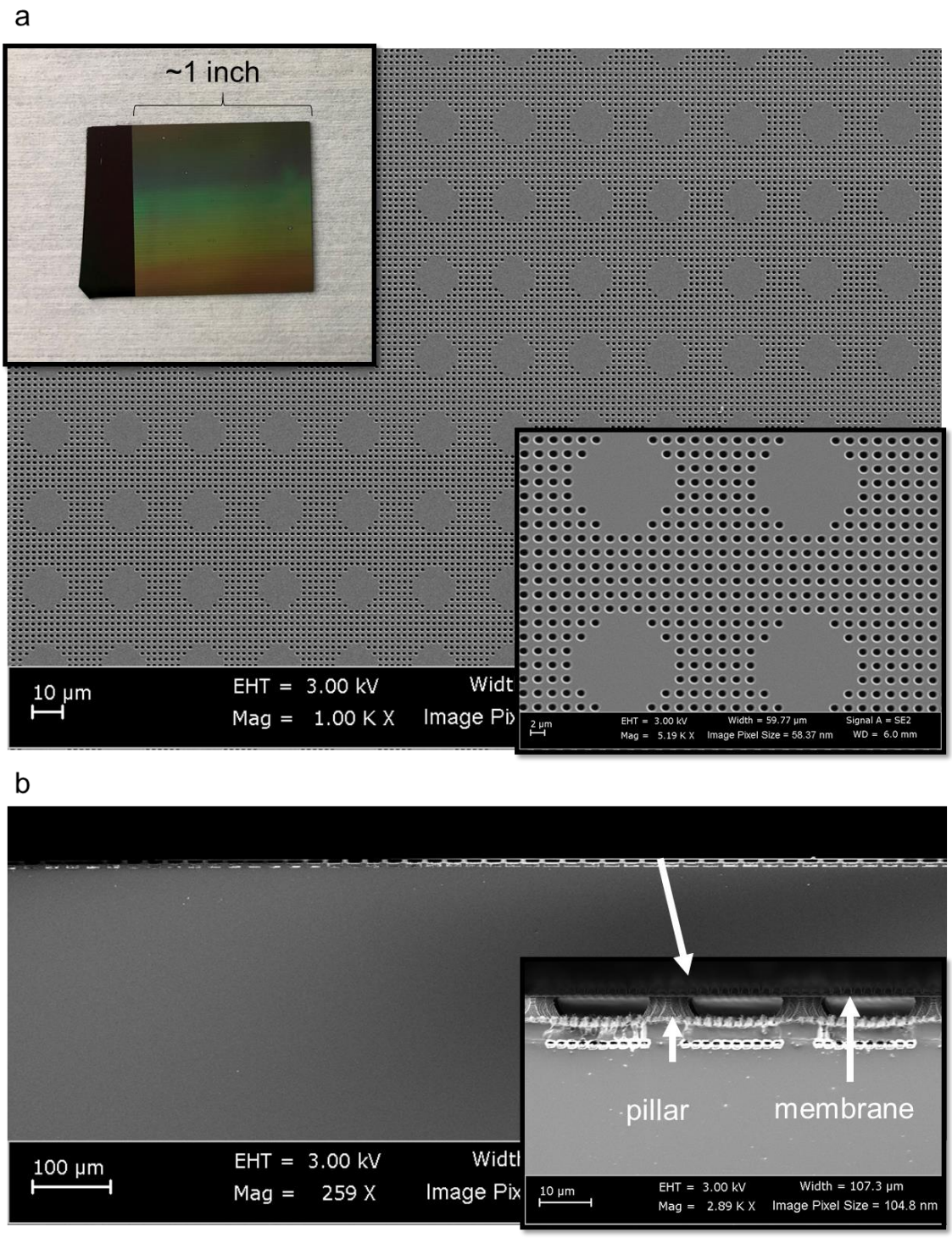

Figure 12. Successful large-scale fabrication of sample. (a) Plane view SEM image of best sample, showing uniformity in structure at larger areas than previously. The top

left inset shows a photograph of the sample, while the bottom right inset shows plane view SEM of a unit cell, showing open pores and pillar locations. (b) Cross section SEM image of best sample showing that the membrane hangs on top of the micropillars for large distances. The lower right inset shows a close up of the structures.

Figure 12 shows scanning electron microscope (SEM) images of the first successful large-scale sample after fabrication. As shown, the surface is uniform and well defined at a low magnification (~1000 x). Note that imaging at even lower magnifications is not ideal since the pattern is not discernible. Nonetheless, the inset at the top left corner shows our successfully fabricated sample at large scale. The characteristic length scale is ~ 1" inch. Note that diffraction from the sample surface looks visibly uniform indicating structure uniformity (and an open wicking layer) across the entire sample. The lower right inset shows a unit cell image with well-defined and open pores. Figure 12(b) shows a cross-section SEM image of the sample. The magnification was sufficiently high to resolve that the membrane hangs on top of the micropillar structure and contains an open space at large-scale. The inset on the lower right shows a close-up of the successful structure. The main components for the hierarchical structure for capillary condensation are achieved, namely, an open wicking structure, and a porous membrane attached on top. Thus, the structure is viable to test during condensation. However, we note that the bottom of the wicking layer contains undesirable residue material which reduces the permeability of the wick. Therefore, we realized that a process had to be developed to achieve opening the wicking structure completely to more closely match the design. Notwithstanding, we may still utilize such a structure for test and study. However, we have solved this incomplete isotropic etching by developing an appropriate recipe in the tool. This has been detailed in past reports and is omitted here for brevity. The samples tested for heat transfer measurements are without this residue layer.

Selectively Coating the Top Surface of Our Sample

In order to achieve capillary-driven condensation with our newly fabricated hydrophilic structure, we search for a simple and effective methods to coat our membrane hydrophobic for condensation tests. For the greatest simplicity, we thought to simply coat the entire sample hydrophobic in a one step method. After all, nucleation is expected to occur everywhere on a subcooled surface. Therefore, we believed that nucleation would occur inside of the wicking structure, and that

nucleates would grow in the structure and connect as a continuous condensate film. However, as we will see later, this was not the case. Although it is the easiest coating method, this configuration turns out to be neither advantageous nor desired. Thus, instead of coating our entire structure hydrophobic, we resolved to develop a method to coat only the top surface of the membrane hydrophobic. This way, a bi-philic structure would be formed where part of the membrane was hydrophobic while the rest of the structure remained hydrophilic. In this configuration, we expected our wicking layer to fill naturally with condensate.

To selectively coat our structure, we first protect areas we do not want coated hydrophobic. Figure 13(a)-(c) shows a process we developed for protecting such regions. First, we show a long slender sample and test the capillary rise height for various viscosities of photoresist. We tried the SPR-220 photoresist series and wicked in 220-1, 220-3, and 220-7. We found that the capillary rise height was not sufficient in either of the SPR-220 series photoresists for our purposes (we require at least ½" inch rise). Therefore, we sought to further decrease the viscosity of the photoresist by diluting it with isopropanol. Figure 13(a) shows that the capillary rise height utilizing a 1:1: ratio of SPR220-1 to isopropanol meets our criteria of a ½" inch rise. Therefore, our strategy is to wick in fluid from two extremes of the sample so that we can protect an entire 1" by 1" sample (Figure 13(b)). We perform a post-wicking bake of our sample at 115 °C for 90 seconds to remove the isopropanol from the structure and leave behind a photoresist layer (Figure 13(c)). Notably, the top surface of the baked sample does not look uniform, but rather has lines indicating areas with more photoresist coverage. We perform SEM imaging of the membrane, the bottom of the wick, and the micropillars to find out how the structure was coated with photoresist. Figure 13(d) shows that the photoresist is able to wick into the membrane pores up to the top surface of the membrane. Figure 13(e) and (f) show that photoresist covers the bottom of the wick and the sidewalls of the pillars with photoresist. To ensure that the top surface of the membrane is not covered with photoresist, we perform an oxygen plasma etch for 20 minutes before applying the hydrophobic coating. Notably, the wick space is not completely filled with photoresist, but all sidewalls inside the structure are covered with a layer of photoresist. This is because the wicked-in solution evaporated in large part, leaving behind a photoresist layer on all walls of the structure. Figure 13(g) shows a schematic of the structure that we are left with after coating. Notably, only the topmost membrane-surface is coated hydrophobic. We utilized a (Heptadecafluoro-1,1,2,2-

tetrahydrodecyl) trimethoxy silane (FAS) hydrophobic coating, which has shown longer durability on silicon based flat surfaces.

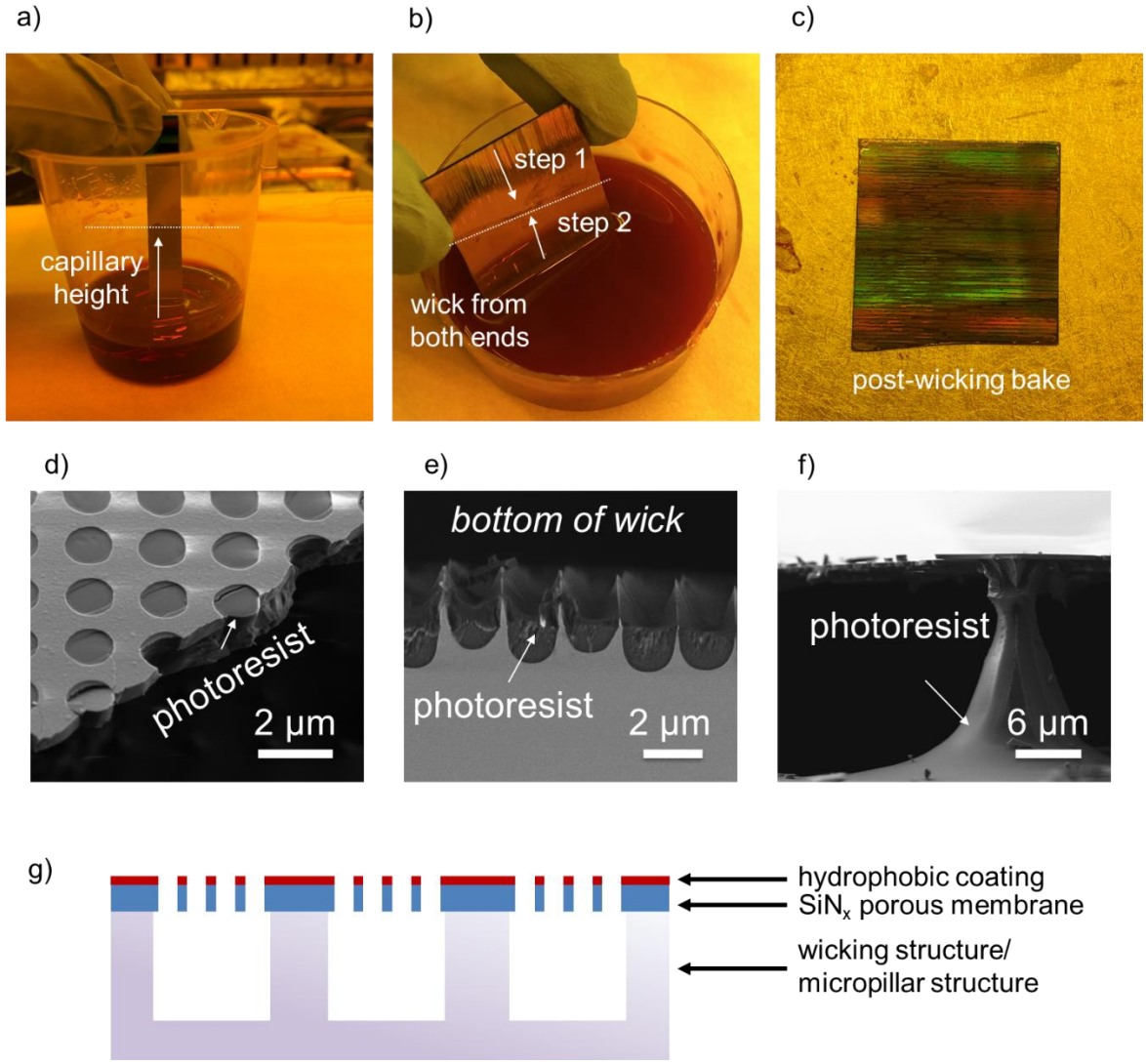

Figure 13. Photoresist-wicking approach to selectively coat our sample hydrophobic a) photoresist is wicked into the structure and rises to a height determined by the photoresist properties b) the large sample is coated with a two-step method where photoresist is wicked in from two sample extremes, c) post-wicking bake shows that distribution of photoresist inside the sample is not uniform, d-f) the photoresist is shown to coat all inside surface of the wick un to the top surface of the membrane, g) schematic of the top-most surface selective hydrophobic coating given by our approach.

Condensation in Ambient Air—Successful Proof-of-Concept and Elucidation of Physics

We built a horizontal test rig on an optical microscope and perform visualization studies of condensation in atmospheric-air conditions at low condensation intensities. Our purpose was to study the interaction of condensate with our biphilic surfaces. Figure 14 shows this setup, whose main components include a chiller loop, a cold stage, a vapor source, and an optical microscope with a CCD camera. The chiller loop consists of a mixture of ice and deionized water that is pumped to the cold stage with a peristaltic pump. The cold stage is a copper plate with welded copper tubing for chilled water flow. A Nikon Eclipse LV100 optical microscope is used to image condensation. In order to increase the intensity of condensation, a water bath was prepared with deionized water which was heated before the onset of boiling to provide enough vapor at around ~ 70º C. The cold stage was maintained at a temperature of ~ 0° C. A dry compressed air line was inserted into this bath to generate bubbles and act as a carrier gas for the vapor. A PixeLINK PL-B742U CCD camera was utilized to record all images and videos. The condensation in this setup is horizontal, meaning that the direction of gravity points towards the front surface of the sample. As a result of this horizontal setup, any droplets on the surface will not shed. The structure visualized during condensation has a pillar diameter of ~15 μm, a pillar pitch of ~150 μm, and a membrane pore size of ~ 1 μm.

Many visualization studies were carried out with various coating techniques. Below, we show results utilizing samples coated with our FAS coating recipe. To begin our visualization study, we first coat our structures in two ways. First, and for ease, we coat our first large-area samples entirely hydrophobic. This means that both the membrane as well as the wick were fully hydrophobic (Figure 15(a)). Typically, such a configuration is discouraged since it ruins the water-wicking capabilities of the structure. However, given that we are not trying to wick in fluid but rather fill the structure with condensate, we expected condensate nucleation to be imminent on hydrophobic surfaces with a sufficiently high subcool and thus naturally fill the wicking structure. However, Figure 15(a) shows that this is not the case. In fact, we observe that such a surface does not fill naturally but forms condensate islands in the wick, rather than a continuous film.

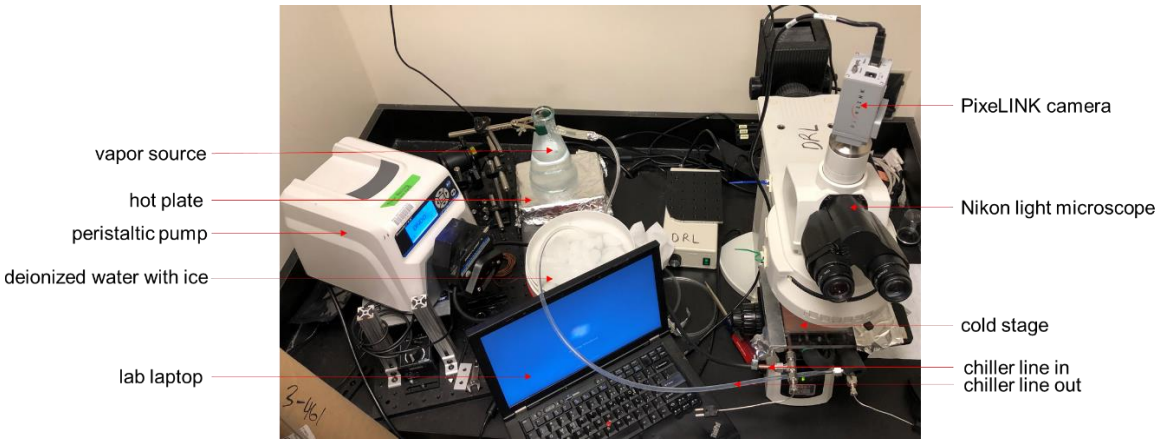

Figure 14. Experimental setup to observe horizontal condensation on structure in ambient conditions under a light microscope under various magnifications. The sample is mounted on top of the cold stage.

First, we can observe that some nucleation appears on the top surface of the sample (left image). As more condensation occurs, we observe that nucleation and coalescence of liquid droplets occurs inside the wicking structure (center image). Here we note that top-surface droplets are absorbed through the membrane pores via liquid bridging between the meniscus pinned at the pore and nearby droplets that can make contact and bridge with the meniscus. Moreover, some droplets remain on the top surface of the membrane and grow. The right-side image shows the formation of small condensate islands inside the wick rather than a continuous film. Further, we observed the incipience of flooding. This occurs in the form of ejected or 'bursting' of droplets from the top surface of the membrane. To explain this phenomenon, we note that the rough hydrophobic wick increases the contact angle of liquid inside the wick, which increases the viscous pressure drop and causes condensate islands to release their pressure by flooding or "bursting" liquid through nearby membrane pores. One down side of these "bursting" droplets is that they strongly pin on the membrane surface. From these observations, we can expect that the heat transfer would be poor since the pinned droplets increase the overall thermal resistance during condensation. Moreover, below the membrane there are large air-filled sections without condensate islands which lower the effective thermal conductivity of the wick. In addition, these regions show no condensate nucleation meaning that heat transfer is not by phase change. Thus, this form of condensation is not advantageous for heat transfer.

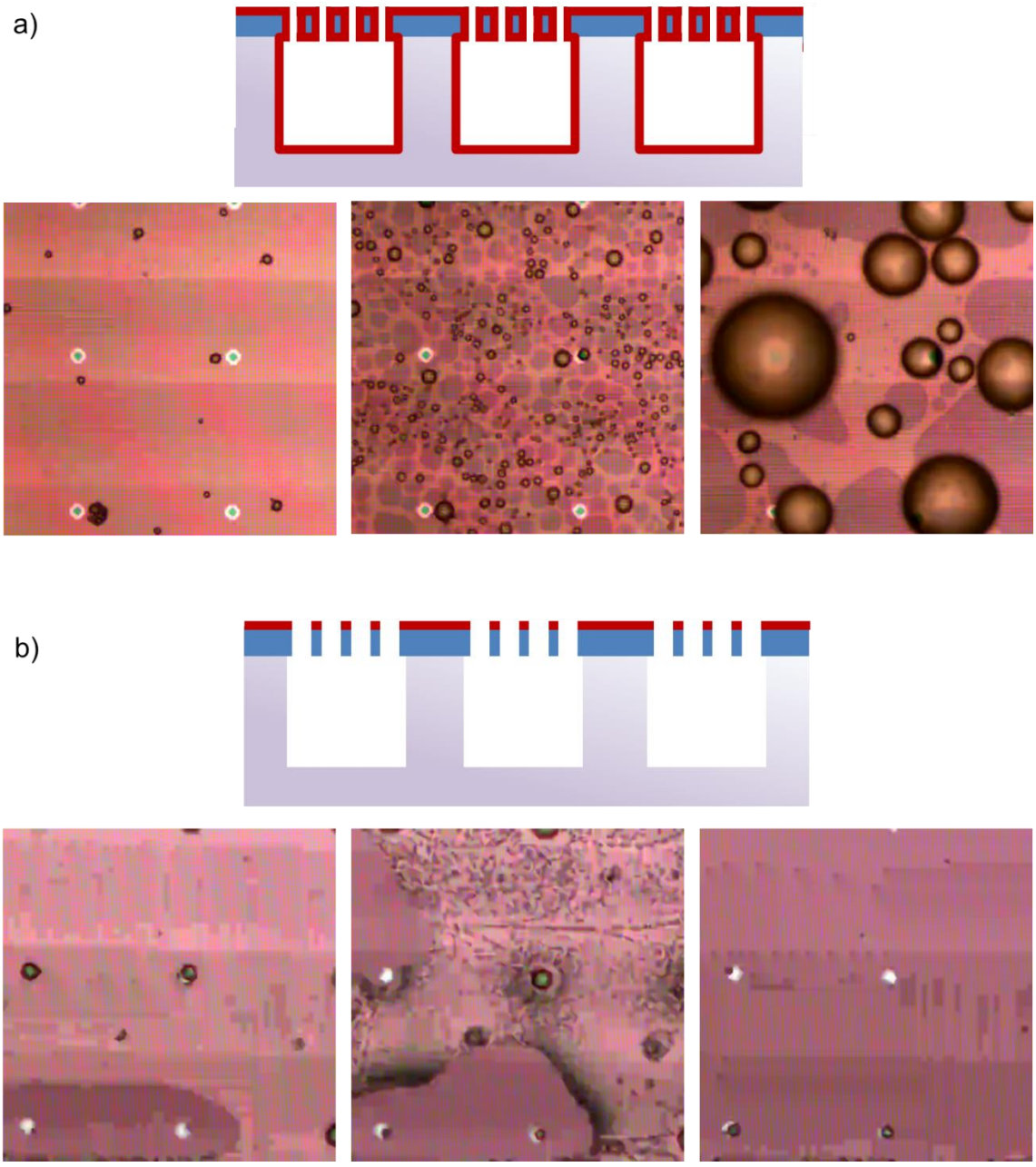

Figure 15. Schematic of coated structure and condensation visualization study under air-ambient conditions for a) a structure coated fully hydrophobic and b) a structure selectively coated such that only the top surface of the membrane is hydrophobic. The red outline in the schematic represents the hydrophobic FAS coating. The pillar pitch in each image is 150 μm.

It is worthy to note that naturally filling the wick with a hydrophobic sample may be possible with taller wicking structures that are less prone to "bursting" droplets. However, such a configuration may lower the HTC. Nevertheless, we conclude that coating the entire structure hydrophobic is

not an advantageous configuration in capillary-driven condensation with the present sample geometry.

Having seen these results, we sought methods to selectively coat the structure, such that the micropillar structure at the bottom of the membrane would remain hydrophilic after fabrication and fill naturally during condensation. We found that our selectively coated surface not only gets rid of top surface droplets on the membrane by continually absorbing them into the wicking structure through the membrane pores, but it also avoids flooding (Figure 15(b)). Moreover, we also found that the new surface can absorb droplets that grow on the top of pillars (**Figure 16**). The droplet base diameter on pillars may only grow to the diameter of the pillar itself before being absorbed through one or more of the surrounding membrane pores. This surface gives the impression of a "dry" condensing surface when viewed at low magnifications.

Visualization experiments comparing the fully hydrophobic samples with our selectively coated samples reveal superior performance and new understanding of the possible operating modes of CDC. Figure 15(b) represents the first successful proof of concept of CDC. Whereas we postulated that there would be vapor transport in the pores in Figure 2, the present results suggest that the mechanism for a dry top-surface is likely direct nucleation of vapor on the top-surface-pinned meniscus, as well as droplet absorption into the wicking structure. Thus, there is liquid rather than vapor transport in the pores. Further, the fluid is removed by capillary pumping from the pinned meniscus at the top of the membrane pore. Thus, we find that CDC may require either i) a meniscus that is pinned at the top surface of the membrane, or ii) a thin enough membrane such that nucleating droplets on the top surface can be absorbed into the structure through liquid-bridging with the pinned meniscus on the pore. Thus, based on our results, naturally filling the wick is necessary to operate our designed sample in the proposed CDC configuration (Figure 2), whether the sample is fully or selectively hydrophobic. Further, by coating the membrane hydrophobic on the structure with the geometry shown, we avoid flooding and the problem of "bursting" droplets and parasitic top surface droplets on the membrane, which decrease the heat transfer performance.

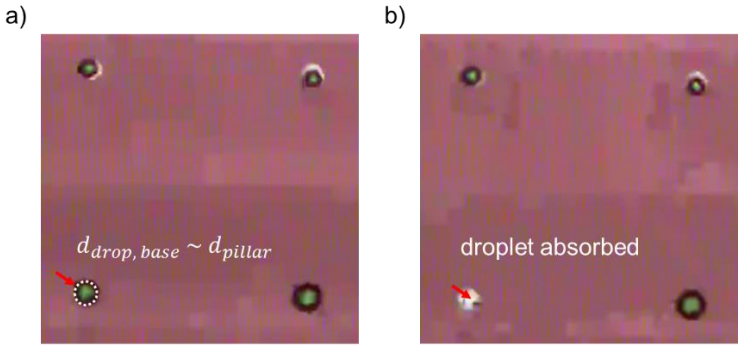

Figure 16. Visualization study of condensation in ambient air showing that droplets that grow on pillar tops can be continually absorbed into the wick through membrane pores and driven to an exit port.

Heat Transfer Measurements in a Pure Vapor Ambient of Selectively-Coated Sample

In this section, we report on our first successful heat transfer measurements of condensation in both a bare copper surface and our engineered CDC sample attached to the copper block. We create a saturated vapor environment at ~ 60 °C. To measure the heat flux, we utilize 5 thermocouple readings along the copper rod at known distances. When the profile is linear at steady state, we take a data point for ~ 10 mins or longer. Figure 17 shows the configuration of the experiments conducted. Notably, there are 5 thermocouples measuring the flux, and 5 measuring the vapor temperature in three different ways. Specifically, two thermocouples measure the vapor temperature directly (dry-bulb), two more measure the temperature of the saturated liquid pool in front of the sample (wet-bulb—small pool), and one measures the temperature of the big water bath filled with condensate. Note that the small pool temperature was always lower than the dry-bulb and liquid puddle temperatures. A steady state point is considered desirable when the agreement between all of the vapor temperatures is close.

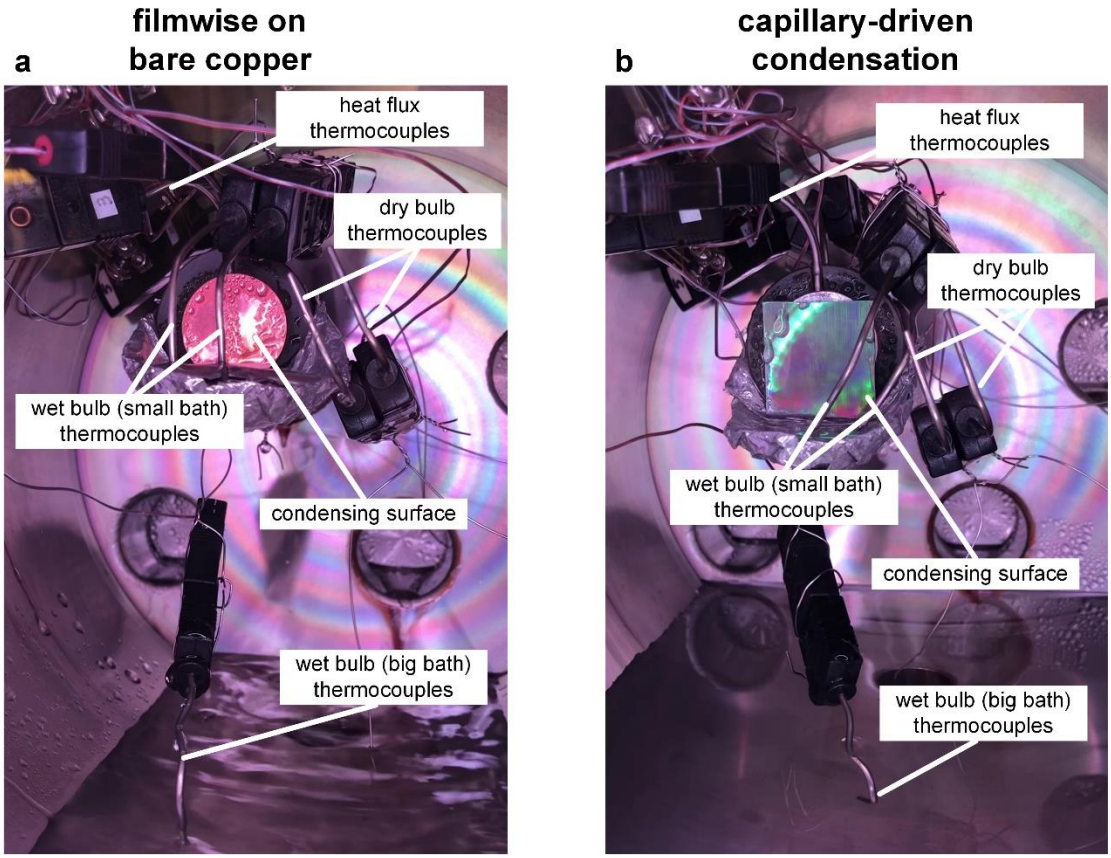

Figure 17. Images showing the experimental configuration for the acquired data. Namely, the experiment is conducted at two saturated vapor conditions for each sample (~ 40 C and ~60 C). (a) image showing the experimental configuration for the filmwise experiment. (b) image condensation on our engineered sample. Notably, a big puddle is formed to promote ensuring a more temperature-stable saturated vapor ambient.

Figure 18 shows data which was collected using the condition mentioned above.

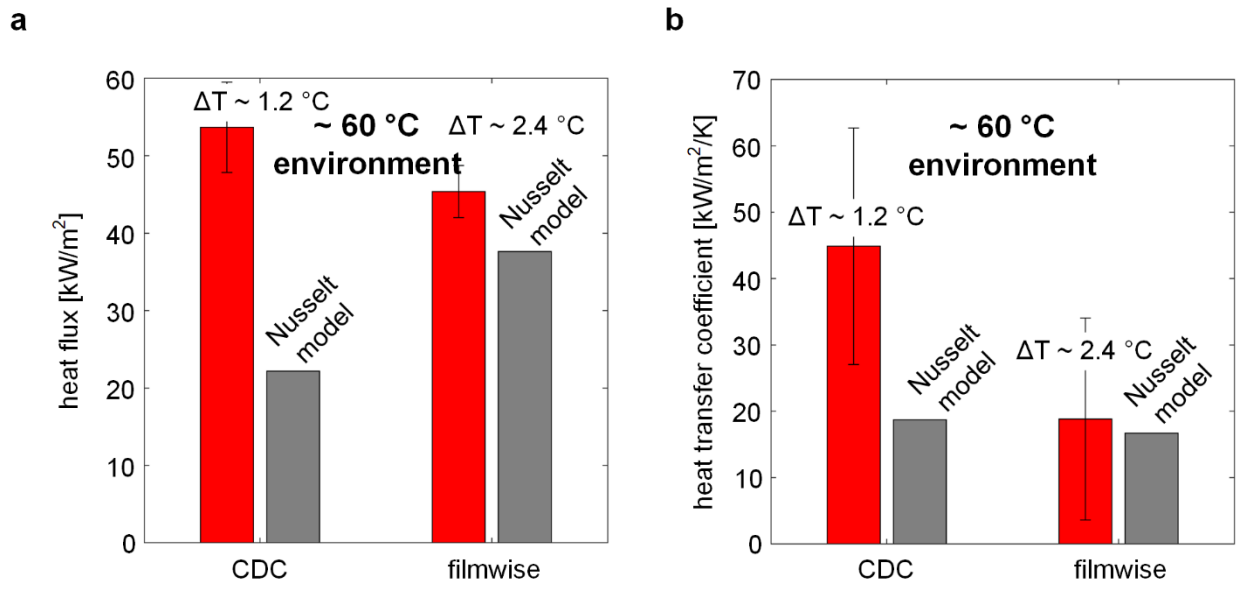

Figure 18. Bar plots of the heat flux (a) and heat transfer coefficient (b). Red bars represent experimentally measured values. Gray bars indicate theoretical predictions of the Nusselt filmwise condensation model at the operating condition. Notably, the data for the experimental filmwise experiments are shown to agree with the theoretical Nusselt model.

Figure 18 plots the heat transfer coefficient and heat flux in bar plots for our experimental condition. Moreover, a Nusselt model theoretical prediction is given for each bar to indicate that the subcool values were not the same for the filmwise and CDC samples at the same experimental condition. Figure 18(a) shows the results for the heat flux. Figure 18(b) shows the heat transfer coefficient results. Notably, there is a 238 % enhancement from ~ 18.84 kW/m^2/K to ~ 44.87 kW/m^2/K in the HTC over filmwise. Note that the error in the HTC for this data point changes significantly over the error of the temperature measurement. Moreover, the measurement is sensitive to the thickness of the bonding layer used to mount the sample, in this case silver epoxy. Minimizing this error will yield more robust measurements since at present the accuracy by which we measure the thickness of this bonding layer presently has a large uncertainty. Future measurements will obtain data points at new conditions, aiming to sweep the subcool range from 0.5 to 6 °C, to more clearly understand the changes in the heat flux and HTC for our samples. In addition, we have two more samples with denser micropillar wicks for which to measure the heat transfer performance and expect higher HTCs.

Figure 19 shows that our surface can achieve a "dry" operating condition where we do not observe droplets coming out from the front of the surface or nucleating and growing on top of the membrane. Rather, there are droplets coming out of the edge of the sample, as designed. Thus, the physics of our proposed concept are further elucidated and confirmed by explicitly showing condensate exiting though the exit port at the edges of the sample, without flooding of droplets through the front surface.

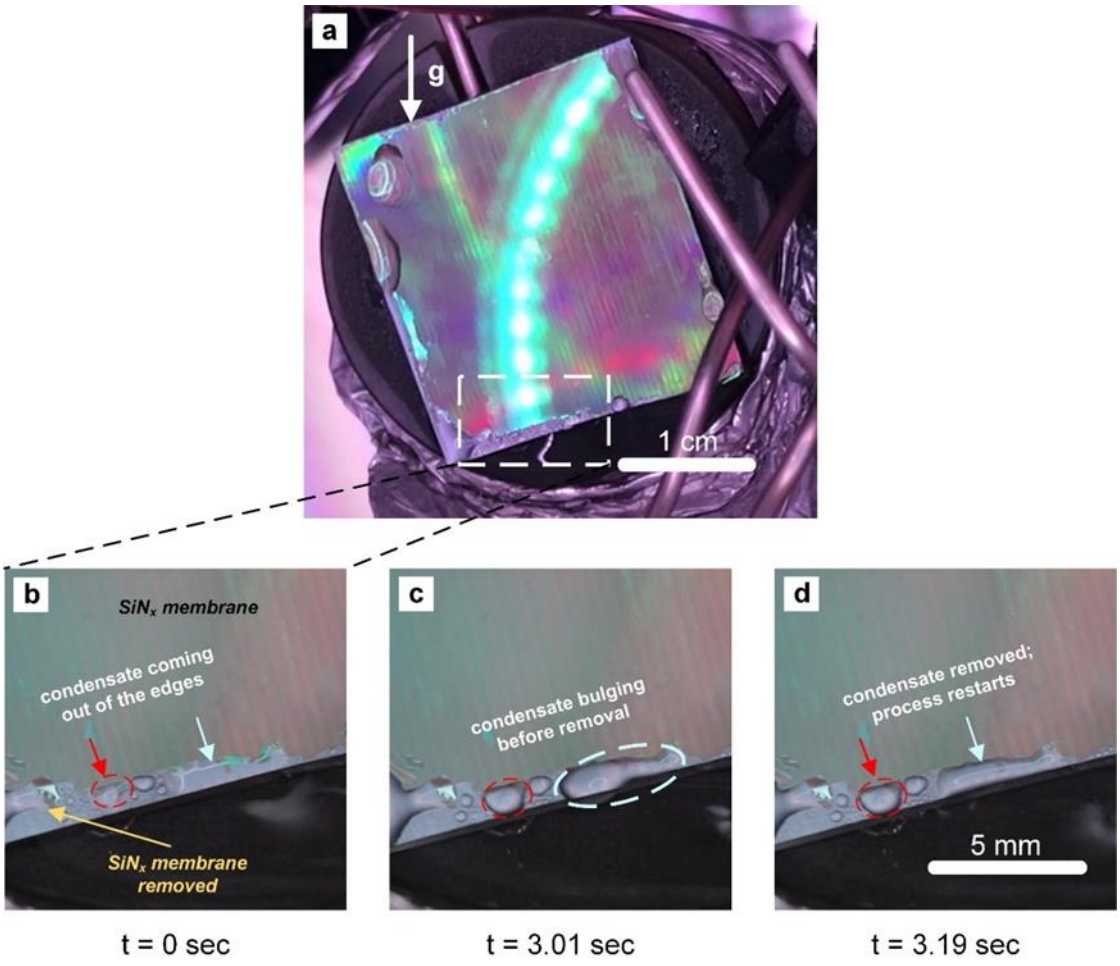

Figure 19. Images showing how the exit port works in our context. (a) Image of a dry-condensation surface at low magnifications. Notably, there are no visible droplets on the surface, or bursting droplets. Rather, vapor condenses on pores in the membrane and is driven to the exit port (edge of the sample). (b)-(d) time-lapse images of fluid exiting from the exit port.

In conclusion, we have modelled, designed, fabricated, functionalized, and tested our silicon-based CDC surfaces with highly defined geometry during condensation in an air-ambient. Most

importantly, we begun measurements of the heat transfer in pure-vapor. We find that we can get enhancements in the HTC of up to ~ 240 % (in a 60 °C saturated vapor environment) compared to the theoretical filmwise condensation prediction for our sample with a sparse micropillar spacing of 150 μm. Further, we expect higher HTC's for the samples with closer micropillar spacing. For future work, we plan to measure the heat transfer on two additional samples with smaller micropillar pitch values. Overall, our samples are seen to lower the temperature drop at the surface or the subcool, which indicates they are lowering the thermal resistance. These results highlight the promise of CDC surfaces in achieving high HTC's. In order to show their promise in a more scalable fashion, the next section concerns the development of scalable CDC surfaces utilizing copper and other scalable materials.

SCALABLE METHODS FOR CAPILLARY-DRIVEN CONDENSATION

For achieving capillary-driven condensation on a large scale, i.e., for application in power plant condensers, our vision is to manufacture a hierarchical condenser tube as shown in **Figure 20** below. A robust (ideally intrinsically) hydrophobic membrane will be combined with a porous, high-thermal-conductivity metal wick and wrapped around the external surface of the condenser tube. During the condensation process, water vapor will transport through the membrane pores and condense inside the porous metal wick, forming a thin film with a thickness constrained by the capillary pressure generated at the base of the membrane pore. Condensed water will be drained out through designated exit port to avoid flooding issue.

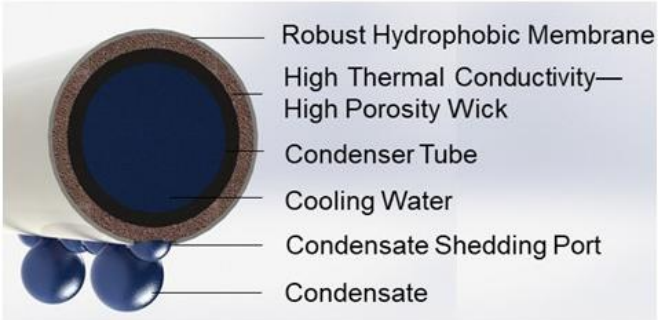

Figure 20. Schematic of a capillary-driven condenser tube. A robust hydrophobic membrane is combined with a high-thermal-conductivity porous metal wick to form a hierarchical structure on the external side of the condenser tube.

Materials Selection

Materials search for hydrophobic membrane

The hydrophobic membrane is a core component of the capillary-driven condenser design, which provides Laplace pressure from the outward-curving liquid-vapor interfaces to drive the condensate transport into the wick structures below the membrane. There are many hydrophobic membrane materials that are commercially available, such as polytetrafluoroethylene (PTFE), polypropylene (PP) and polyvinylidene difluoride (PVDF). A list of some commercially available choices for hydrophobic membranes and their corresponding properties are shown in **Table 2**.

Table 2. Examples for commercially available hydrophobic membranes.

Material	Contact angle of water(°)	Pore sizes (μm)	Thick-ness (μm)	Manufacturer	Price ($/m^2)
PTFE laminated	adv~100, rec~90	0.1-0.2	152-254	Steritech	400-2400
PTFE laminated	adv~100, rec~90	0.2	76-152	Steritech	400-2400
PTFE laminated	adv~100, rec~90	0.45	64-127	Steritech	400-2400
PTFE laminated	adv~100, rec~90	1	76-127	Steritech	400-2400
PTFE unlaminated	adv~100, rec~90	0.2	25-51	Steritech	400-20000
PTFE unlaminated	adv~100, rec~90	0.45	25-51	Steritech	400-20000
PTFE unlaminated	adv~100, rec~90	1	203-305	Steritech	400-20000
PTFE unlaminated	adv~100, rec~90	5	152-254	Steritech	400-20000

PTFE unlaminated	adv~100, rec~90	10	130	Steritech	400-20000
PP	95 (adv~110, rec~90)	0.1	85-115	Steritech	500-800
PP	95 (adv~110, rec~90)	0.2	155-185	Steritech	500-800
PP	95 (adv~110, rec~90)	0.2 (nominal)	170	Steritech	500-800
PP	95 (adv~110, rec~90)	0.45 (nominal)	203	Steritech	500-800
PP	95 (adv~110, rec~90)	1.2 (nominal)	305	Steritech	500-800
PP	95 (adv~110, rec~90)	10(nominal)	152	Steritech	500-800
PVDF	100	0.02,0.1	50	Steritech	4000-10000
PVDF	100	0.02	50	Steritech	4000-10000
PVDF	100	0.1	50	Steritech	4000-10000

PTFE membranes are intrinsically hydrophobic, chemically stable, and applicable to large scale industrial applications. They have a relatively wide range of pore size (0.1-10 μm) and thickness that are commercially available, and their prices vary from several hundred to several thousands of dollars per meter squared depending on the geometry. The unlaminated PTFE membranes do not have a supportive layer, while the laminated ones have a supportive layer of PP or polyester (PE) to enhance the mechanical performance of the membrane. Normally, the supportive layer has ~3x of pore size as that of the selective layer and therefore has better permeability.

Another intrinsically hydrophobic potential membrane material is PP. PP membranes are strong, flexible, and compatible with a broad range of chemicals. They also have a relatively wide range of pore size and thickness that are commercially available, though for large pore sizes (>0.2 μm)

the pores are no longer absolutely cylindrical and the nominal pore size is used as a representation. PP membranes have similar range of costs as PTFE membranes.

PVDF membranes are also intrinsically hydrophobic, though they have relatively higher prices as compared to other membrane materials. PVDF has been widely used in large scale industries such as membrane distillation, oil-water separation, batteries, and tissue engineering.

Although variety of hydrophobic membranes are available on the market, few of them fulfill our requirement for membrane pore size and thickness. As we will discuss in the later part of this report, we ended up fabricating the PVDF membranes using a customized electrospinning setup in order to optimize membrane properties for efficient capillary-driven condensation. By the use of electrospinning, we can control the pore size and the thickness of the PVDF membrane and significantly lower down the cost of the PVDF membrane to several dollars per meter square surface area.

Materials search for porous metal wick

The wick structure is the other core component of the capillary-driven condenser design, which reduces the thermal resistance through integrating the condensate liquid film with a high-thermal conductivity structured wick of a required thickness.

Various types of structured metal wicks are available commercially. For example, metal wire cloth, perforated sheets, and metal foams with different thickness and porosity can be easily found on the market, as shown in **Table 3**. Compared to wire cloth, perforated sheets are more rigid and durable for a longer service life in harsh environments. However, both wire cloth and perforated sheets are closed-cell structures that constitute individual enclosures. On the other hand, metal foams consist of cells that are all interconnected, allowing the condensate fluid to pass through the wicking structure.

Table 3. Examples for commercially available porous metals.

Material	Volumetric porosity (%)	Thickness (µm)	Pore/ grid size(µm)	Mesh size (grids per inch)	Metal thermal conductivity (W/(mK))	Manu-facturer	Price ($/m^2)
Perforated metals							
perforated stainless steel	22-31	127-356	152-508	-	15	McMaster-Carr	520-1300
perforated brass	20-48	406	>=508	-	100	McMaster-Carr	<=400
perforated steel	20-63	>=457	>=609	-	50	McMaster-Carr	<=151
perforated aluminum	23-58	>=813	>=1588	-	200	McMaster-Carr	<=70
Wire cloth							
copper wire cloth	30	114	152	100	385	McMaster-Carr	80
copper wire cloth	30	190	229	60	385	McMaster-Carr	103
nickel-copper wire cloth	34	53	74	200	22	McMaster-Carr	256
steel wire cloth	25-36	>=203	>=229	1-60	50	McMaster-Carr	<=140
316 stainless steel wire cloth	12-82	25-2032	38-11500	1-400	13	McMaster-Carr	40-330
Metal foams							
Copper foam	50-98	1600	100-1000	5-120	385	MTI Co.	2743
Copper foam	70-80	80	-	-	385	MTI Co.	2708
Nickel foam	>=95	1600	250	80-110	90	MTI Co.	506

In addition to metal foams, sintered powder wicks are another widely used option for metal wick structures. In fact, approximately 80% of conventional heat pipes use sintered powders as wick structures[16]. Similar to metal wicks made of metal mesh/wire clothes, sintered metal powder can provide large capillary force but relatively low liquid permeability as compared to metal foams.

The effective thermal conductivity k_{eff} of the porous metal wick is crucial to the heat transfer performance of the capillary-driven condensation. The metal's thermal conductivity and its volumetric porosity are critical to k_{eff}. Copper has the best thermal conductivity among all the listed materials and has a mid-range price. Higher porosity of the porous wick would decrease its k_{eff}, although the wick permeability κ, which is desirable for condensate flow, increases with increasing pore size and porosity. When designing the wick structures, careful consideration needs to be made on the porosity and the pore size of the structures to ensure good balance between κ and k_{eff}.

The arrangement of the metal network could also affect k_{eff}. Highly connected metal structures like copper foams usually have higher k_{eff} than those with poorer connections even at the same porosity. **Figure 21** shows the comparison among effective thermal conductivities of different metal structures.

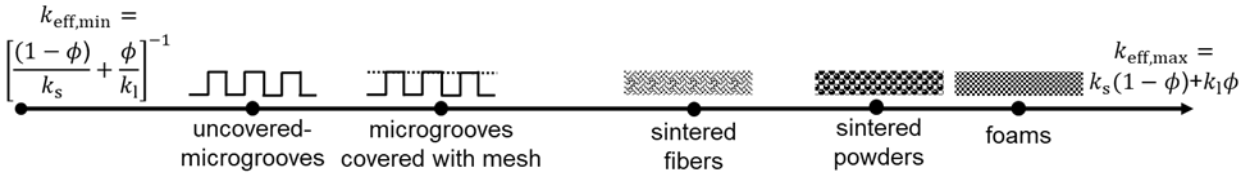

Figure 21. Comparison of effective thermal conductivities among different metal structures (assuming at the same porosity).

The thickness of the metal wicks determines the thickness of the condensate film and therefore plays an important role in the condensation heat transfer performance. Commercially available metal wicks such as copper foams usually have a thickness above 200 μm, limiting the heat transfer performance of the wick layer. Porous metal wicks can be fabricated through electrodeposition, such as electrodeposited copper foam shown in **Figure 21**[17]. This technique can tune the thickness of the porous metal wick through controlling the deposition time and can also be applied to large scale.

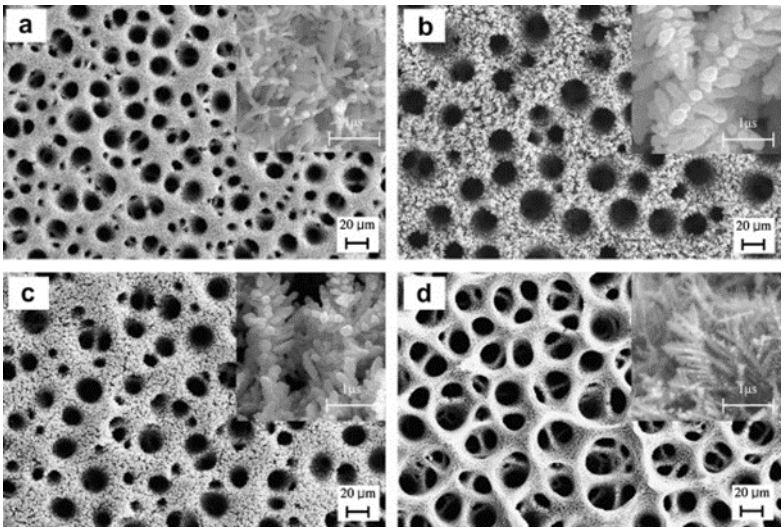

Figure 22. 3-dimensionally interconnected spherical pore network by electrodeposion[17].

As we will show in the next section, we started with commercially available copper foams with the smallest thickness available on the market and used them as porous copper wick for proof of concept. Besides, we have also developed porous copper substrates with much smaller thickness based on electrodeposition.

Proof of Concept based on Commercially Available Materials

We selected two commercially available materials for the scalable proof-of-concept study. Porous copper foams with a thickness of ~200 μm (thinnest we could find on the market) and porosity of ~70% were purchased from MTI Co. and used as the wick layer. Copper meshes with different mesh sizes (i.e., 200 mesh size, 500 mesh size, and 1500 mesh size) were purchased from TWP Inc. and Structure Probe Inc., and used as the membrane layer after hydrophobic coating. The advantages of using hydrophobized metal meshes as the membrane layer for the proof-of-concept study are (1) metal meshes are relatively easy to be bonded to the metal wick layer; (2) metal meshes with well-defined pore sizes are commercially available; (3) hydrophobic coating has well-developed deposition procedure and its lifetime (typically 1~2 days) is long enough to experimentally validate heat transfer enhancement. Detailed properties of the two layers of materials are shown in Table 4 below.

Table 4. Properties of the copper meshes and copper foams chosen for the proof-of-concept study.

Copper mesh membrane					Copper foam wick		
mesh size	wire diameter	pore size	porosity	thickness	permeability	thickness	porosity
200	50.8 μm	80 μm	0.35	112 μm	1E-11 m^2	200 μm	65%
500	11.4 μm	39 μm	0.6	5 μm			
1500	5.6 μm	11 μm	0.44	5 μm			

Sample fabrication via diffusion bonding

We started fabricating capillary-driven condensers based on a 1-inch diameter copper block, which was fabricated by mechanically and then chemically polishing the end of a copper block followed by solvent and acid cleaning the surface. In order to obtain good thermal contact between the copper condenser block, the copper foam wick, and the copper mesh membrane, we diffusion-bonded the copper foam and the copper mesh to the copper block using a furnace.

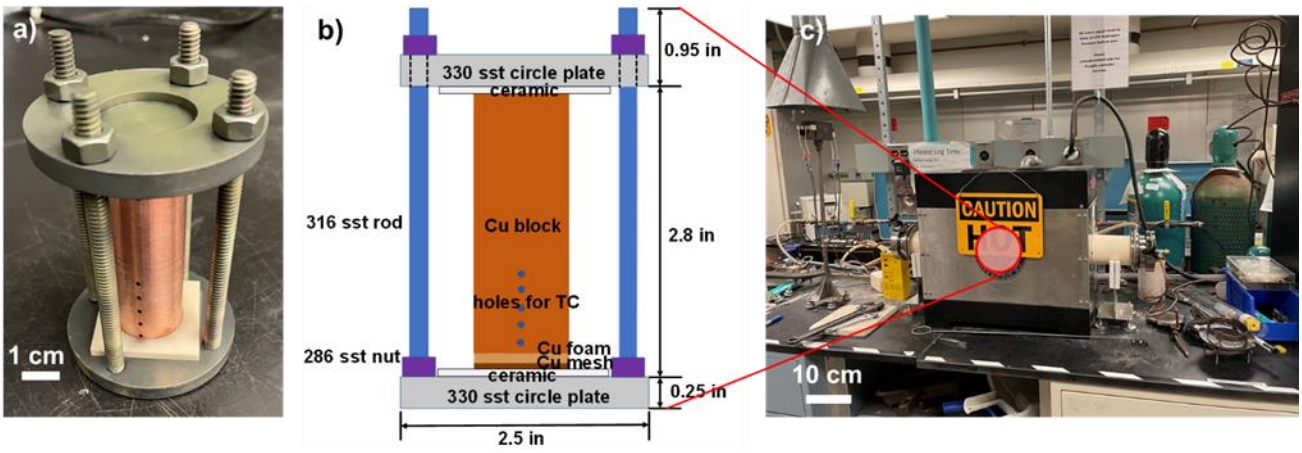

Figure 23. Diffusion bonding assembly and the high temperature furnace for diffusion bonding. (a) and (b): an image and a schematic of the diffusion assembly. (c) An image of the high temperature furnace.

A schematic and an image of the latest diffusion bonding assembly are shown in **Figure 22** (a) and (b). The copper block condenser substrate, the copper foam, and the copper mesh with the same diameter (1 inch) were aligned one by one in between two thin (0.125 inch-thick) ceramic plates, which have a shallow dent of 1.02-inch-diameter circle in the middle for the copper parts to fit in. The use of the ceramic plates is to prevent possible diffusion bonding from occurring between the stainless-steel clamp and the copper. The slightly larger diameter of the dents on the ceramic plates

is to accommodate the thermal expansion of the copper parts under the high temperature during the diffusion bonding process. The two ceramic plates with the copper parts between them are clamped together by a pair of customized stainless-steel parallel clamps. Using different types of stainless steel can prevent diffusion bond from occurring among the stainless-steel parts under high temperature. The torque applied on the nuts can generate a uniform clamping pressure over the stainless-steel parallel plates, assisting gravity force to hold the three copper parts together during the diffusion bonding process.

Three different hierarchical copper surfaces were designed and fabricated through diffusion bonding, as shown in the scanning electron microscopy (SEM) images in **Figure 23**. For the wick layer of all three sample surfaces, we used the same copper foam with a measured permeability of over 1E-11m^2 and a thickness of ~200 µm. For the membrane layer, three different types of copper mesh were selected for the three sample surfaces: 200 mesh size copper wire cloth (TWP Inc.), 500 mesh size electrodeposited copper mesh (Structure Probe, Inc.), and 1500 mesh size electrodeposited copper mesh (Structure Probe, Inc.), which correspond to pore sizes of ~80 µm, ~40 µm, and 10 µm, respectively. More details about the geometrical properties of the selected copper foams and copper meshes are shown in **Table 4**.

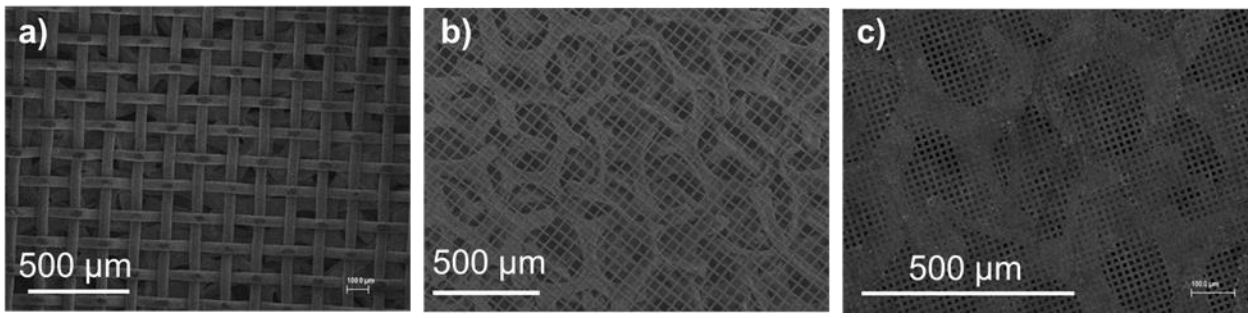

Figure 24. SEM images of the 3 hierarchical copper surfaces made by diffusion bonding a 200 µm thick copper foam with: (a) a 200-mesh-size copper mesh; (b) a 500-mesh-size copper mesh; (c) a 1500-mesh-size copper mesh.

We measured the permeability of the wick layer of our hierarchical copper samples, which is the 200µm-thick copper foam, under various processing conditions, such as different pressure for the diffusion bonding/hot press procedure and different heating time for the sample to be kept in the high temperature furnace. The permeability measurement was conducted by following an established procedure described in the literature[18]. **Figure 24** shows 4 examples of the permeability measurement we have done.

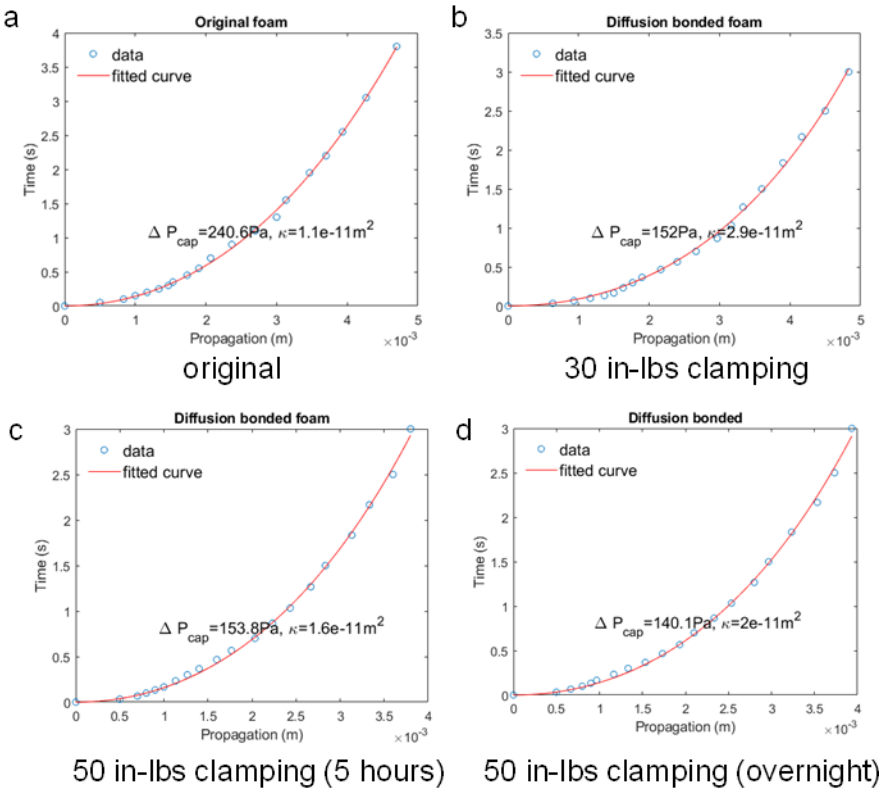

Figure 25. Permeability characterization of the wick layer under various processing conditions.

Figure 24(a)-(d) show the permeability measured on the (a) original copper foam, (b) copper foam being diffusion bonded/hot-pressed with 30 in-lbs torque clamping force applied on the diffusion bonding assembly, (c) copper foam being diffusion bonded/hot-pressed with 50 in-lbs torque clamping force applied on the diffusion bonding assembly and with a total processing time of 5 hours in the furnace, and (d) copper foam being diffusion bonded/hot-pressed with 50 in-lbs torque clamping force applied on the diffusion bonding assembly and with a total processing time of over 10 hours in the furnace. By comparing Figure 26(a) with the other three figures, we found that permeability increases after the diffusion bonding/hot press procedure. This is potentially a result of the oxidation of the copper structures during the heating process along with the etching of copper oxides by HCL treatment after the diffusion bonding/hot press step. Furthermore, we found that keeping the sample under high temperature for a longer time would slightly increase its permeability. On the other hand, increasing the clamping force on the diffusion bonding assembly would decrease the permeability of the sample, as shown by Figure 27 (b) and (c). All samples we tested have permeabilities on the order of 1E-11 m^2. Therefore, we chose 1E-11 m^2 as a

conservative estimation for the permeability of the copper wick/foam and adopted this value into our heat and mass transfer model.

Coating method

For the proof of concept study, the membrane layer was fabricated by hydrophobizing the copper mesh. The hydrophobic coating was achieved vapor deposition using FAS ((Heptadecafluoro-1,1,2,2-tetrahydrodecyl) trimethoxy silane) to form conformal hydrophobic coating on metal surfaces. This specific coating exhibits a consistent water contact angle of ~105°.

The details of the coating procedure are as follows. First, we cleaned the copper sample with acetone, ethanol, isopropanol, and water in sequence to remove potential hydrocarbon contaminants. Then, we dipped the sample in to an HCL solution (0.2 M) for 30 seconds to remove oxides. After the samples are rinsed with water and dried with nitrogen, we oxygen plasma cleaned the sample for 20 minutes. With bombardment of air plasma, the copper surface would be more active and easier to form a conformal coating. Then, we put the sample into a sealed bottle. Along with the porous copper samples, we also put 800 μL of FAS in toluene solution (5 V%) into a small beaker, which sat beside the samples to be coated. The sealed bottle was placed in an oven at 100°C for 3 hours, during which the FAS was coated onto the porous copper sample via vapor phase deposition. Finally, the samples were taken out of the furnace and cooled down to room temperature in the fume hood. A schematic of the coating process in illustrated in **Figure 28**.

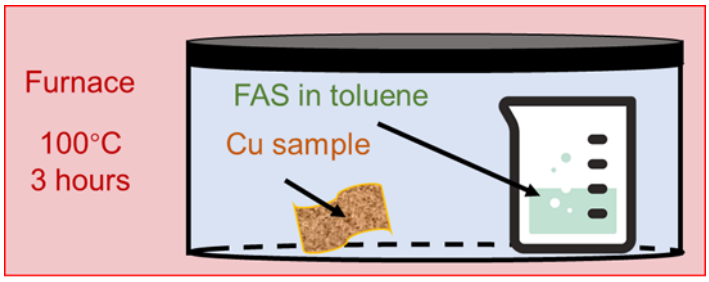

Figure 28. Vapor deposition of FAS on porous copper sample.

Ideally, only the copper mesh layer needs to be hydrophobized for the proof-of-concept study, and the copper foam layer should remain hydrophilic to promote condensation nucleation. Biphilic coating can be made by depositing hydrophobic coating when covering the bottom-layer structures with a protective coating which can be washed away easily after the hydrophobic coating. For this

study, we applied biphilic coating to the hierarchical copper sample by utilizing a heat curing photoresist (AZ3312) as the protective layer for the copper foam structures. The detailed procedure includes following steps. First, we cleaned the sample with acetone, ethanol, isopropanol, and water, followed by 10 minutes of argon plasma cleaning. Then, we dipped the sample into a beaker of photoresist AZ3312 and allowed the photoresist to climb up into the porous copper under capillary force. Once we ensured that all the copper foam area was covered by photoresist, we baked the sample in an oven at 100°C for 10 minutes until the photoresist was solidified inside the porous copper sample. Next, we applied 20 minutes of oxygen plasma to remove the top layer photoresist off the hierarchical sample, exposing the hydrophilic copper mesh to be hydrophobized. The photoresist-protected hierarchical copper sample was then deposited with FAS coating using the procedure illustrated in **Figure 28**. Finally, we ultrasonically cleaned the hydrophobized hierarchical copper sample with acetone to remove the photoresist residue and recovered the hydrophilic copper foam layer. Condensation on hydrophilic surfaces enables a lower nucleation barrier as compared to hydrophobic ones[19]. As a result, the biphilic coating ensures condensation start from the hydrophilic copper foam and then reach the hydrophobic mesh layer.

Micro-channels for condensate exit

Although the permeability of the copper foam (1E-11m^2) was low enough to prevent flooding at low surface subcools, flooding could potentially occur at local defects such as broken mesh pores, which was hardly evitable during the fabrication process. In order to further facilitate condensate drainage, we machined microchannels on the copper foam layer, as shown in **Figure 29**. Only one end of the microchannels was machined all the way done to the edge of the sample to ensure directional condensate flow. The channel width, channel depth, and distance between the microchannels were selected as 100 μm, 100 μm, and 1.27 mm, respectively. These dimensions were chosen based on the tools available and were used for a test study. Further modeling is needed to optimize the design of the microchannels.

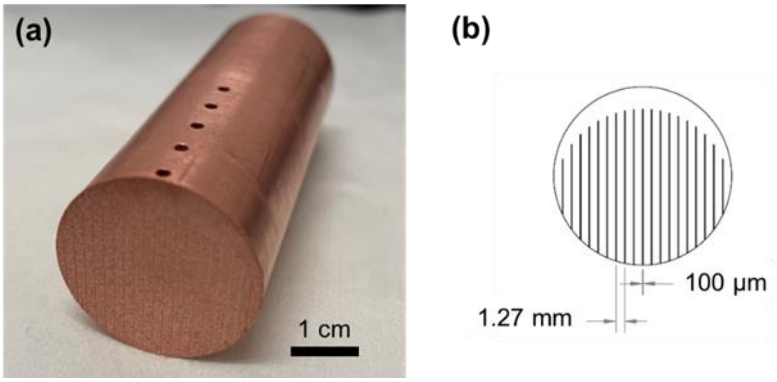

Figure 29. Image (a) and schematic (b) showing a copper foam sample machined with microchannels for condensate drainage. Channel width: 100 μm; channel depth: 100 μm; distance between neighboring channels: 1.27mm.

Heat and mass transfer model

We developed an analytical model based on 1D conduction through liquid-filled porous copper to predict the heat transfer performance of the three hierarchical sample surfaces. To calculate the effective thermal conductivity of a copper mesh, we adopted the following equation, which is developed and validated by previous literature[20]:

$$k_{\text{eff,mesh}} = \frac{\beta-\varepsilon}{\beta+\varepsilon} k_l \quad (18)$$

$$\beta = (1+\frac{k_s}{k_l})/(1-\frac{k_s}{k_l}) \quad (19)$$

where ε is the volume faction of the solid phase. k_s is the thermal conductivity of the solid (copper), and k_l is the thermal conductivity of the liquid (water).

The effective thermal conductivity of the wick layer (copper foam) can be calculated using the volumetric average value as been shown in previous literature[18]:

$$k_{\text{eff,wick}} = \varepsilon k_s + (1-k_s)k_l \quad (20)$$

Heat flux and fluid flow were analytically solved under an environmental condition with vapor temperature of 35°C and surface subcool up to 5°C. This vapor condition is normally seen in steam power plant condensers and we are aiming to achieve this condition during our experiments. Conventional filmwise condensation heat transfer predicted by the Nusselt model is used as the benchmark. **Figure 30**(a), (b), and (c) show the model-predicted heat transfer performance of the

three samples: (1) 200-mesh-size copper mesh covered copper foam, (2) 500-mesh-size copper mesh covered copper foam, and (3) 1500-mesh-size copper mesh covered copper foam. The y axis on the left shows heat flux, and the y axis on the right shows the flooding criteria P^*, which is the ratio of the viscous pressure loss for condensate to travel through the wick layer and the capillary pressure given by the hydrophobized mesh pores. In order to prevent flooding from happening, we should operate the experiments within the regime $0<P^*<1$. Otherwise, flooding would occur and greatly deteriorate the heat transfer performance of the condensing surface. **Figure 30**(a) shows that, although the 200-mesh-size sample would not flood throughout the subcool regime we are investigating (0-5°C), it only gives marginal enhancement on the heat transfer as compared to the filmwise condensation on a flat surface. This is due to the large thickness of the 200-mesh-size sample (>20x thicker than the other two samples), which significantly decreases the effective thermal conductivity of the mesh layer and consequently reduces the heat transfer coefficient of the system. **Figure 30**(b) shows that, the 500-mesh-size sample could greatly enhance the heat transfer performance as compared to the conventional filmwise condensation, yet only within a narrow range of subcool (0~1.5°C). Flooding would occur on the 500-mesh-size sample once the subcool is larger than ~1.5°C. This is due to the large mesh pore size of the 500-mesh-size sample (~4x larger than the 1500-mesh-size sample), which limits the capillary pressure that drives the condensate to flow throughout the wick layer. The 1500-mesh-size sample has the smallest mesh pore and the smallest mesh thickness among the three samples, which results in its significant heat transfer enhancement (>10x) within a relatively wide subcool regime (0~4.1°C), as shown in **Figure 30**(c).

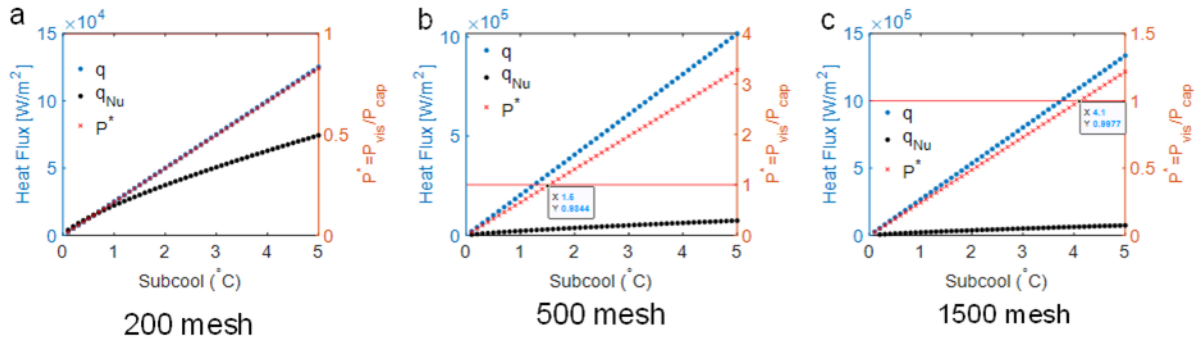

Figure 30. Heat transfer enhancement given by the three hierarchical copper surfaces predicted by the analytical model.

Condensation heat transfer experiment

We experimentally characterized heat transfer performance of the fabricated sample surfaces in a controlled environmental chamber, as shown in **Figure 31**. The sample copper block was installed onto a test rig inside the chamber, as shown in **Figure 31**(a). An array of five thermocouple probes were inserted into the copper block along its length to monitor the temperature distribution along the copper block. Assuming 1D (linear) conduction heat transfer, heat flux flowing through the copper block could be extracted from the temperature measurements by Fourier's Law. The linear fit for the temperature measurements had an R^2 value of over 99% for each measurement throughout our experiments, indicating that the assumption of linear conduction was valid and heat transfer through the block walls was negligible. The back side of the copper block was cooled with chiller water provided by an external chiller (Fisher Scientific Isotemp II), and the front side of the copper block, where the hierarchical copper surface was attached to, was served as the condenser surface. The temperature at the condenser surface (right below the copper wick layer) was determined by extrapolating the linear temperature distribution along the copper block measured by the thermocouple array.

A Pirani gauge was installed on the chamber to accurately monitor the chamber pressure under pumping process, as shown in **Figure 31**(b). Before every experiment, we pumped the chamber below 0.5Pa to eliminate non-condensable gases (NCGs). Following removal of NCGs, pure, degassed vapor was introduced into the chamber from a heated, temperature-controlled water reservoir (as shown in **Figure 31**(c)), and allowed to condense on the condenser surface. The vapor pressure inside the chamber was manually maintained at a constant (~5.3 kPa) by opening the valve on the reservoir and measured by another pressure transducer installed on the chamber (Omega, MMA030V5B3MB0T3A5CE). Two thermocouples were installed inside the chamber to measure wetbulb and drybulb temperature, respectively. When at steady state, these two temperature agreed with each other with a discrepancy falling under the uncertainty of the thermocouple readings (0.15 °C). Then, the experimentally measured condensation heat transfer coefficient was determined by dividing the heat flux by the surface subcool. For each data point, we waited for over 30 minutes to make sure steady state was reached, and the data point was collected by averaging measurements over a time span of 5 minutes. Visualization of the

condensation development was achieved through a viewing window on the chamber, where a camera was placed towards the viewing window outside the chamber.

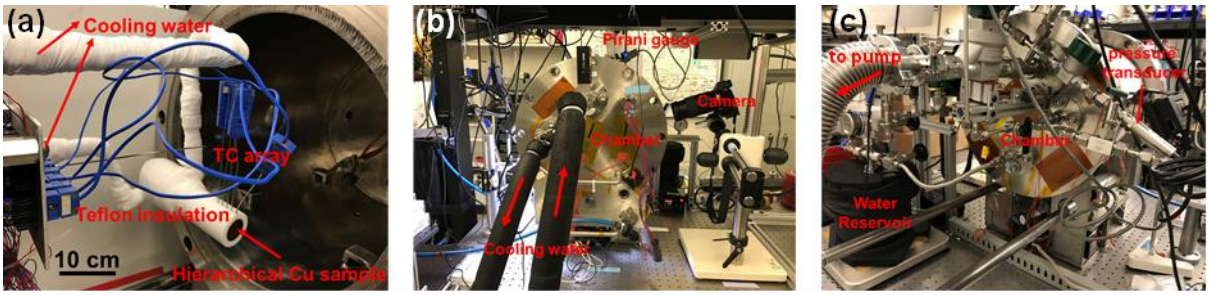

Figure 31. Images taken inside (a) and outside (b-c) the environmental chamber.

Condensation heat transfer on a flat copper surface was measured and compared to the Nusselt model prediction to validate the capability of the environmental chamber. **Figure 32** shows the experimental results of condensation on a flat copper surface. A flat condensate film was observed throughout the experiment, as shown in **Figure 32**(a). We measured the condensation heat flux under 6 different subcool conditions ranging from 0.3-7 °C, as shown in **Figure 32**(b). All the measured data points (red dots) are in good agreement with the Nusselt model prediction for filmwise condensation heat transfer (blue curve), validating that the chamber and the experimental procedures are capable of taking reliable measurements.

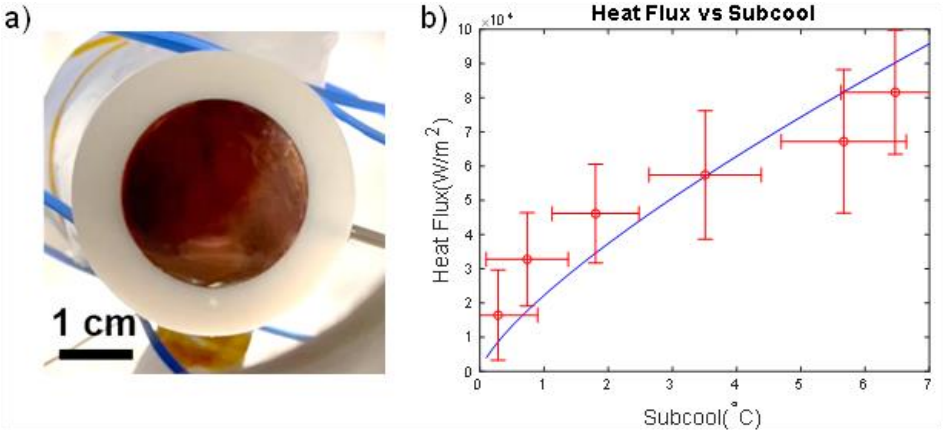

Figure 32. (a) Filmwise condensation on a flat copper sample and (b) the corresponding heat transfer data.

For the proof of concept study, we tested three hierarchical copper samples, all of which were based on 1500-mesh-size copper mesh covered copper foam structures. Samples with different

wettability (i.e., fully hydrophobic and biphilic) were tested to investigate the influence of surface wettability on the condensation heat transfer performance.

Figure 33 shows the experimental results of condensation on a fully hydrophobic hierarchical copper sample. **Figure 33**(a) shows that the sample was completely dry and kept under vacuum before we introduced water vapor into the chamber. At the beginning of the condensation experiment, we set the chiller temperature to 5 °C, which induced a large subcool on the sample surface and initiated condensation. Nucleation of condensation was observed everywhere on the top of the fully hydrophobic hierarchical copper sample in a pattern similar to dropwise condensation on a hydrophobic surface, as shown in **Figure 33**(b). As condensation continued (after the first few seconds), water started to fill into the interconnected pores inside the copper foam layer, and drained at the bottom of the surface due to gravity. Capillary force generated at the hydrophobic copper mesh layer was able to keep majority of the surface free of droplets, though flooding was observed on certain locations probably due to local defected mesh pores, as shown in **Figure 33**(c). **Figure 33**(d) shows the heat flux measured on the fully hydrophobic hierarchical copper surface under different subcooling. Due to the existence of the bursting droplets which could act as resistance to heat transfer, the heat transfer performance of this sample was just as good as filmwise condensation.

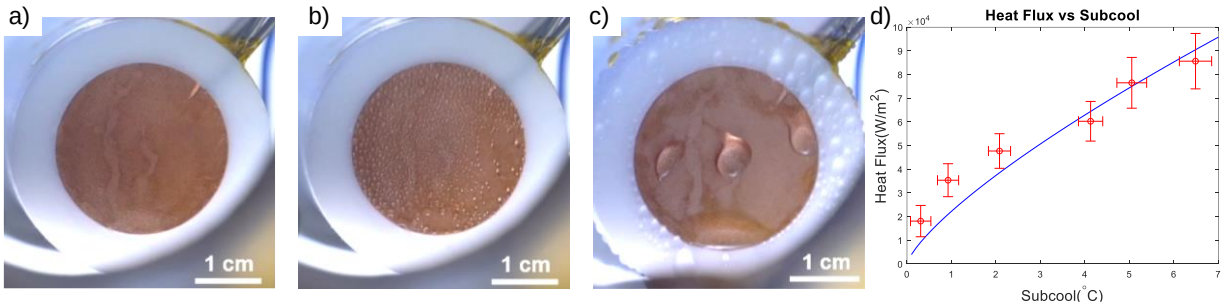

Figure 33. Condensation experiments on fully hydrophobic hierarchical copper sample and the resulting heat transfer performance. (a)-(c): images of the sample inside the chamber before condensation occurred (a); at the very beginning of the condensation experiment (b); at later stage of the condensation experiment (c). (d): heat flux measured on the sample under various subcools (red data points) in comparison with Nusselt model prediction for filmwise condensation heat transfer (blue curve).

Figure 34 shows the experimental results of condensation on a biphilic hierarchical copper sample. **Figure 34**(a) shows that the sample was completely dry and kept under vacuum before we introduced water vapor into the chamber. We repeated the experimental procedure as the previous

experiment by first setting the chiller temperature to 5 °C. Interestingly, we did not observe the random pattern of condensation nucleation on the top of this biphilic hierarchical copper. Instead, droplets started to burst out from several locations, as shown in **Figure 34**(b). As condensation continued (after the first few seconds), water started to fill the interconnected pores inside the copper foam layer, and condensation on this biphilic sample started to show the similar capillary-driven pattern as the fully hydrophobic sample, which demonstrated that capillary-driven condensation would occur as long as the top layer membrane is hydrophobic. Capillary force generated at the hydrophobic copper mesh layer was able to keep majority of the surface free of droplets, though flooding was observed on certain locations probably due to local defected mesh pores, as shown in **Figure 34**(c). **Figure 34**(d) shows the heat flux measured on the fully hydrophobic hierarchical copper surface under different subcooling. Again, due to the existence of the bursting droplets, the heat transfer performance of this sample was not better than filmwise condensation.

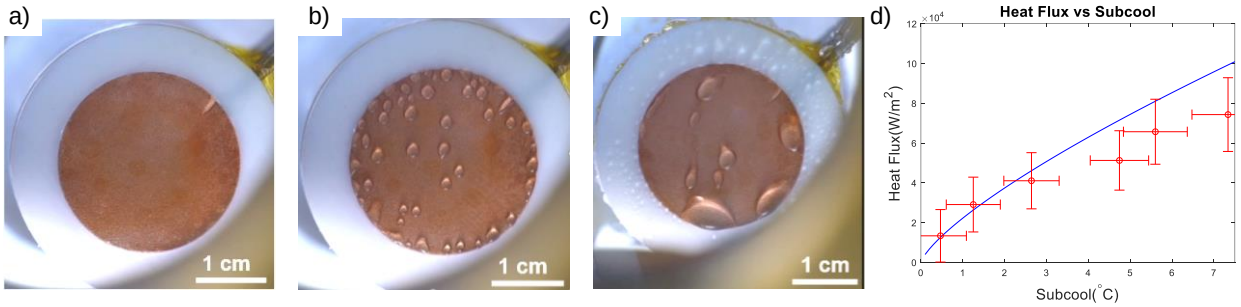

Figure 34. Condensation experiments on biphilic hierarchical copper sample and the resulting heat transfer performance. (a)-(c): images of the sample inside the chamber before condensation occurred (a); at the very beginning of the condensation experiment (b); at later stage of the condensation experiment (c). (d): heat flux measured on the sample under various subcools (red data points) in comparison with Nusselt model prediction for filmwise condensation heat transfer (blue curve).

Figure 35 shows the experimental results of condensation on a biphilic, micro-channeled hierarchical copper sample. **Figure 35**(a) shows that the sample was completely dry and kept under vacuum before we introduced water vapor into the chamber. The same experimental procedure as the previous experiments was repeated on this sample. Similar to the biphilic hierarchical copper sample, this biphilic micro-channeled hierarchical copper sample also showed local flooding/bursting droplets at the very beginning of the experiments, as sown in **Figure 35**(b). As condensation continued (after the first few seconds), condensation on this biphilic sample started to show the similar capillary-driven pattern as the previous two samples, as shown in **Figure 35**(c).

Interestingly, the capillary force generated at the hydrophobic copper mesh layer was able to keep most of the surface free of droplets, enabling a condensing surface free of droplets, as shown in **Figure 35**(c). This was achieved by having the micro-channels as additional exit ports. The flow resistance through the microchannels was lower than the bursting pressure of most broken mesh pores. Therefore, even there were local defects on the copper mesh layer, we did not observe many bursting droplets on the top of the surface. **Figure 35**(d) shows the heat flux measured on the biphilic, micro-channeled hierarchical copper surface under different subcooling. On this biphilic hierarchical copper sample, the heat transfer performance was measured to be 50% better than filmwise condensation.

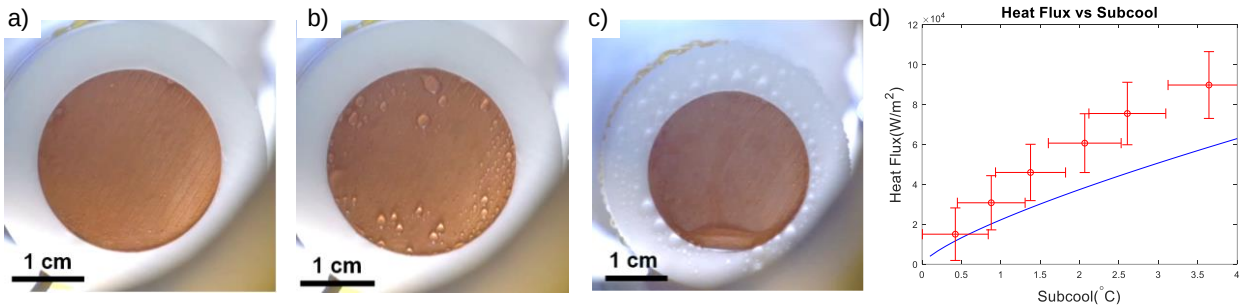

Figure 35. Condensation experiments on biphilic, micro-channeled hierarchical copper sample and the resulting heat transfer performance. (a)-(c): images of the sample inside the chamber before condensation occurred (a); at the very beginning of the condensation experiment (b); at later stage of the condensation experiment (c). (d): heat flux measured on the sample under various subcools (red data points) in comparison with Nusselt model prediction for filmwise condensation heat transfer (blue curve).

The 50% enhancement measured on the biphilic hierarchical copper sample was promising, although it was lower than what we expected from our model prediction. The following reasons are our hypothesis for the discrepancy between the modelling results and the experimental results. (1) The micro-channels decreased the effective thermal conductivity of the copper foam layer, which was not captured in our model; (2) The copper foam we purchased had a poor connection in its vertical direction as compared to its horizontal direction, but the vertical direction was critical for the heat transfer experiment. Therefore, the effective thermal conductivity of the copper foam was overestimated by calculating a volumetric average value. (3) There were inevitable defects such as broken pores in the copper mesh layer due to the diffusion bonding process. These defects would affect flooding criteria and heat transfer performance. We did not consider those defects in the model. Thermal conductivity of the micro-channelled hierarchical copper sample needs to be

measured or estimated using a more accurate model. The design of the microchannels (channel width, channel height, distance between nonboring channels) also requires further modelling guidance. Combining a thinner copper wick layer with an optimized microchannel structure is expected to further enhance the heat transfer performance of the capillary-driven condenser.

Fabrication of Hydrophobic Membrane in a Scalable Way

In an effort to fabricate a scalable, robust, and cost-effective capillary-driven condenser, we started to fabricate intrinsic hydrophobic membranes based on electrospinning. Electrospinning is a sophisticated technique for fabricating nano- and microfiber membranes, which has been applied to various industries such as water desalination, oil separation, and water harvesting. We see the potential of using electrospinning to directly deposit fibres atop porous metal wick to fabricate capillary-driven condensers in a scalable way.

Electrospinning PVDF-HFP membrane

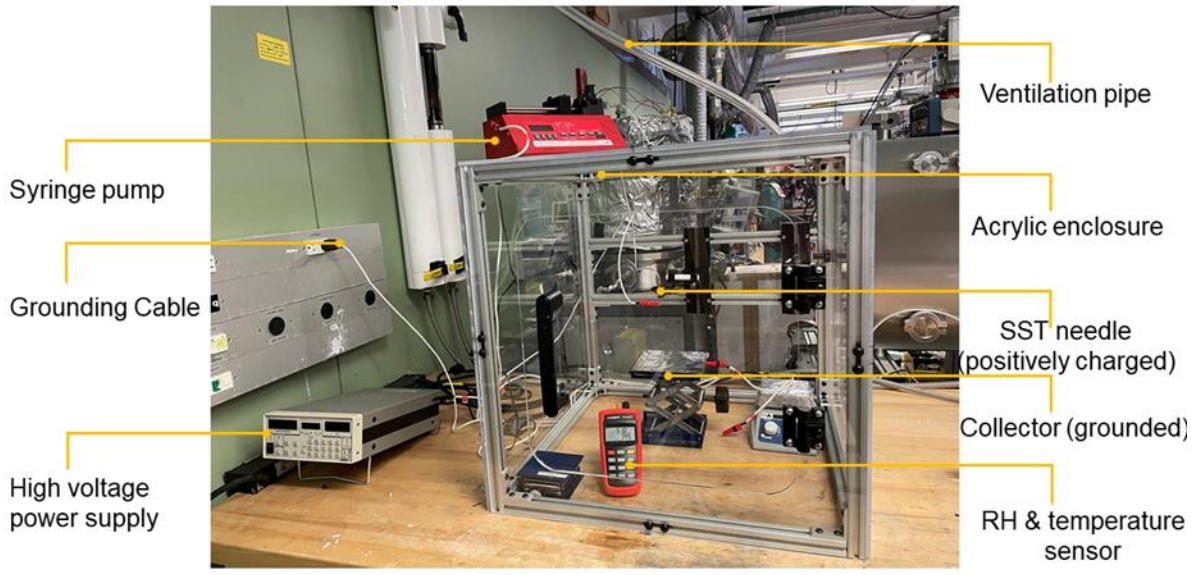

Figure 36. Customized electrospinning setup for fabricating hydrophobic membranes.

We built a customized electrospinning set up, as shown in **Figure 36**. Two major components of the electrospinning setup are the high voltage power supply and the syringe pump. A polymer solution (PVDF-HFP in our current test) is loaded onto the syringe and extruded from the needle tip where a positive charge is applied. An aluminium foil covered copper plate is used as the fiber collecter and is connected to a ground wire. The high voltage difference across the needle and the

collector drives the polymer solution to spin onto the collector in a form of nano- or microfibers, under the counteractions of electrostatic force and surface tension experienced by the solution. The electrospinning process involves many operation parameters, some of which are critical to the fiber/membrane fabricated by the process. Some key parameters include voltage being applied, distance between the needle and the collector, concentration of the polymer solution, and the time the electrospinning process lasts. We focus on electrospinning PVDF-HFP since this polymer is intrinsically hydrophobic and is known to form uniform membrane pores.

Characterization of membrane properties

Three properties of the membrane are critical to vapor transport and heat transfer through the membrane layer: pore size, thickness, and porosity. For electrospun fibrous membranes, the pore size is usually proportional to the fiber diameter. In order to characterize these important properties, several techniques were used as detailed below.

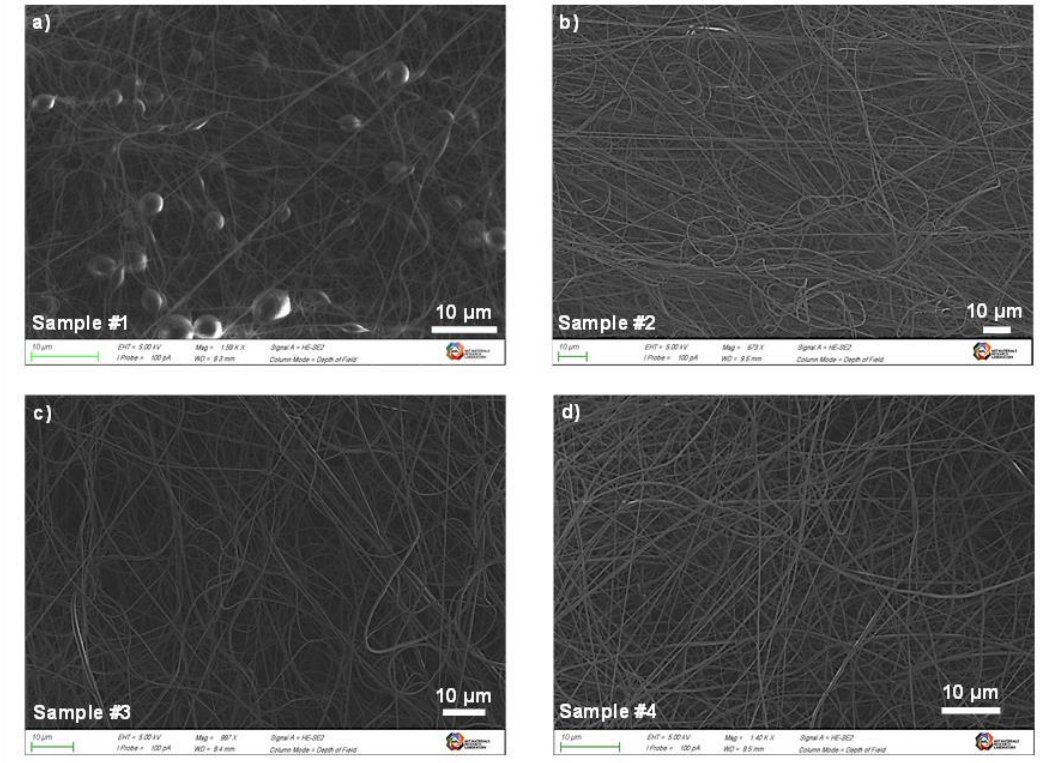

Figure 37. SEM images of electrospun membrane samples. Fiber diameter and morphology can be characterized accurately using SEM. However, pore size distribution is hard to define due to the random alignment of the fibers.

Scanning electron microscopy (SEM) images were taken to help us characterize the morphology of the electrospun fibers, as shown in **Figure 37**. SEM images could clearly show important information of independent fibers (e.g., fiber diameter, presence of beads) and how the fibers are being aligned into a membrane. However, due to the random alignment of the electrospun fibers, it was hard to characterize pore size of the membrane using SEM. However, pore size distribution is an important info we need in order to predict the capillary pressure that the membrane can generate and the vapor transport resistance through the membrane. Therefore, in addition to the SEM, we used a capillary flow porometry (POROLUX™ 1000) to characterize pore size distribution and gas permeability of the electrospun membrane.

Figure 38 shows how a capillary flow porosity works to get the pore size distribution. We first wetted our sample membrane with a known fluid (Galpore, surface tension 15.6 mN/m) and put it into the porometer for the wet curve measurement. During the measurement, a nitrogen flow was applied to the membrane sample with incremental pressure difference across the membrane. At each pressure, flow rate of nitrogen gas was recorded. At the beginning of the measurement, flow rate stayed at zero since all the pores were blocked by the liquid. At one point, nitrogen started to flow through the membrane, which denoted that the biggest pore inside the membrane (i.e. bobble point pore size) was opened up by the gas flow. After this point, the nitrogen gas flow rate would keep increasing until a point when the smallest pore inside the membrane was open, i.e., the membrane became completely dry. Following the wet curve measurement, another round of gas flow rate measurement was repeated on the dry sample with the same incremental pressure being applied, resulted in a dry curve. A curve with 50% of the dry curve slope was plotted as “half-dry curve”, as shown in **Figure 38**. Pore size at which 50 % of the total gas flow can be accounted (half the flow is through pores larger than this diameter) is defined as the mean flow pore (MFP) diameter. Pore size distribution could be extracted from the wet curve and dry curve measurements, as shown in **Figure 39**.

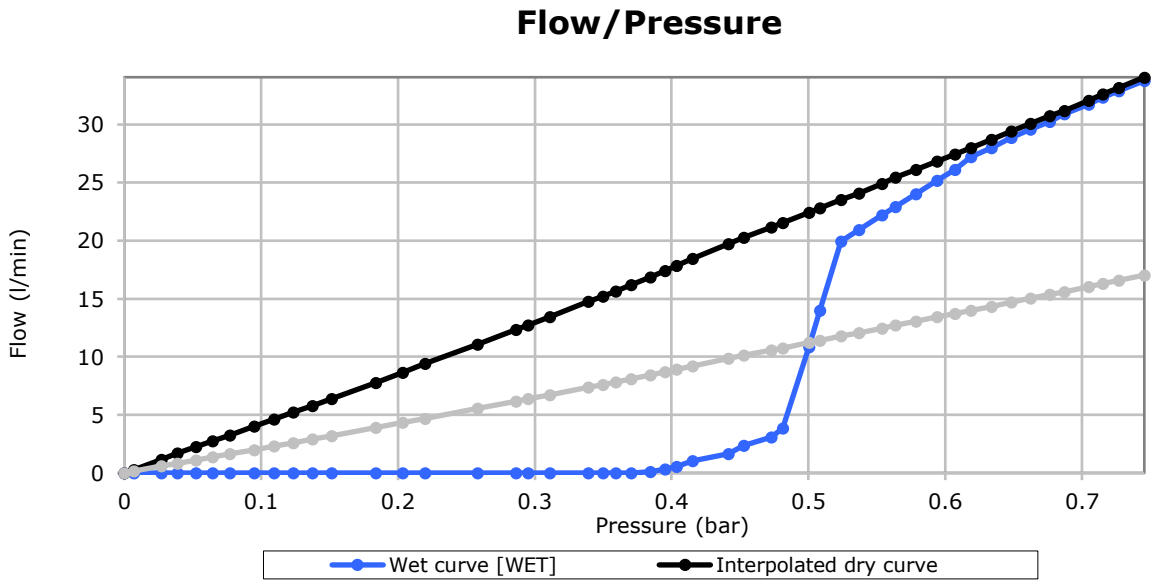

Figure 38. Wet curve and dry curve of an electrospun membrane sample given by the capillary flow porometer (Porolux 1000).

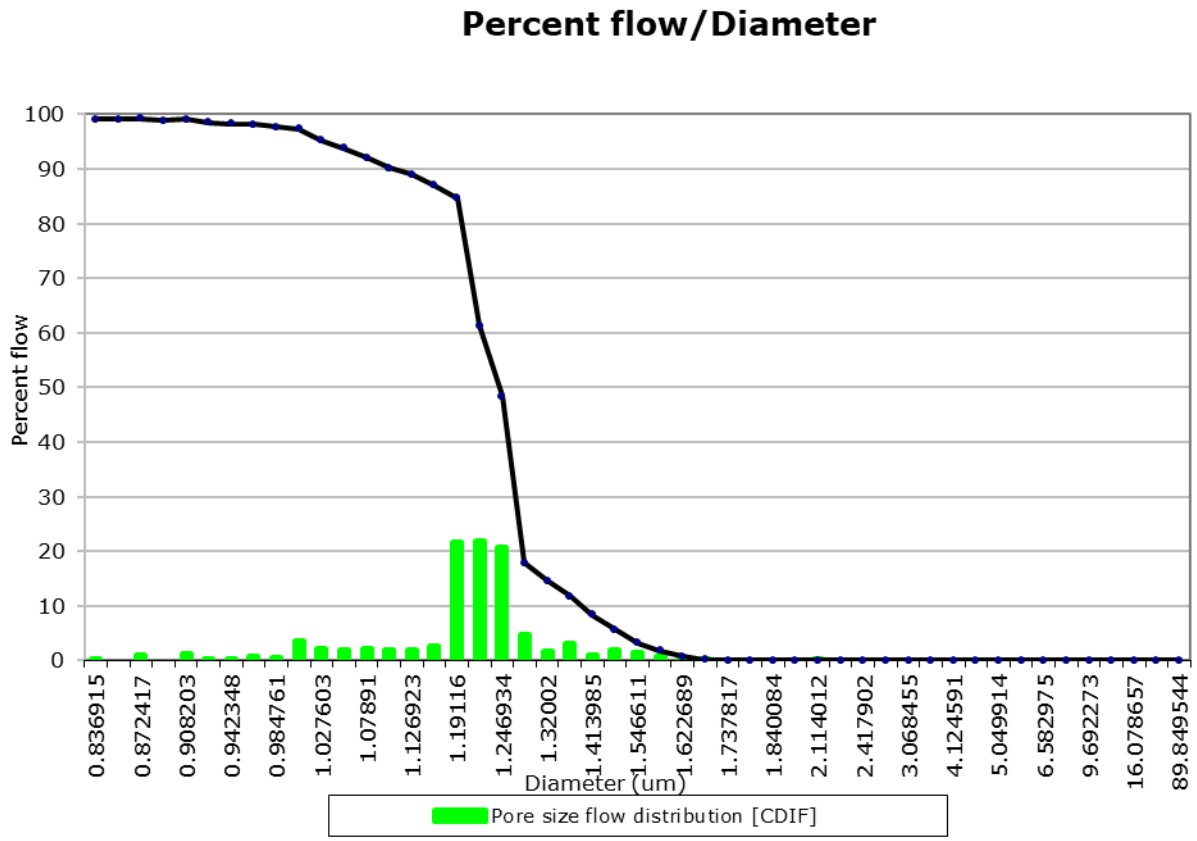

Figure 39. Pore size distribution of an electrospun membrane sample given by the capillary flow porometer (Porolux 1000).

The thickness of the membrane was measured by a micrometer with a resolution of 1 μm. We calculated the average of three independent thickness measurements at the thickest part of the electrospun membrane and used it as the membrane thickness. In addition, we measured the membrane weight and the membrane surface area to calculate membrane porosity. A consistent porosity of ~ 80% was obtained through all of our PVDF-HFP samples, which is in good agreement with the literature[21].

Factional factorial design for parametric optimization of electrospun membranes

We started an optimized parametric study on the electrospinning process based on fractional factorial design (FFD). In statistics, fractional factorial designs are experimental designs consisting of a carefully chosen subset (fraction) of the experimental runs of a full factorial design. **Figure 40** is an example of the reduced number of combinations in a fractional factorial design[22]. The filled circles in **Figure 40**(a) correspond to the eight runs in the calculations in a full factorial design. The filled circles in **Figure 40**(b) correspond to the four performed runs of the eight possible in the calculations in a fractional factorial design.

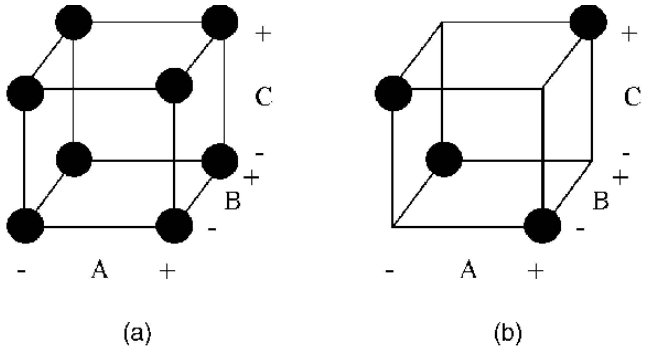

Figure 40. An example of the reduced number of combinations in a fractional factorial design [22].

The FFD method we used in this study varied factors together and fitted the results using a polynomial method. It could determine how factors interact, but could have errors due to polynomial assumption. Therefore, we used FFD for screening parameters before we moved on to full factorial study on the most important parameters.

During the screening study, we studied the effects of the four important fabrication parameters, namely the voltage supply, the discharge/needle distance, the solution concentration, and the

syringe pump's feeding rate on the morphology of the electrospun membrane. **Table 5** shows the first 8 samples we fabricated as guided by the fractional factorial design.

Table 5. Fractional Factorial Design (FFD) for screening.

Pattern	Voltage Supply (kV)	Needle Distance (cm)	PVDF Concent. (wt%)	Feeding Rate (ml/hr)	Fiber size (um)		Pore size		Thickness (μm)		Porosity
					avg	sd	MFP (μm)	N2 permeability (μm^2)	avg	uncertainty	
+−−+	20	15	10	1	0.128	0.033	0.8559	1.2	50	10	0.8
+−+−	20	15	20	0.1	0.372	0.099	3.852	1.4	6	5	0.79
−++−	10	20	20	0.1	0.346	0.093	2.073	2.9	17	5	0.91
++++	20	20	20	1	0.281	0.093	1.245	1.6	60	20	0.81
−−−−	10	15	10	0.1	0.266	0.071	2.467	1.5	12	3	0.8
++−−	20	20	10	0.1	0.288	0.116	2.477	1.2	7	5	0.82
−−++	10	15	20	1	0.615	0.392	1.62	3	100	25	0.79
−+−+	10	20	10	1	0.265	0.089	1.323	1.4	30	15	0.78

As shown in **Table 5**, porosity does not change much throughout the screening tests. As we will shown in the later section, a 10% change in membrane porosity would not affect much on the heat transfer performance of the capillary-driven condenser. Therefore, we focused on the influence of the four parameters on the membrane pore size and the thickness. Note that thickness could be adjust by changing the electrospinning time. As a result, the most important resulting property is the membrane pore size.

We plotted the results in **Table 5** with the four parameters (i.e., voltage supply, needle-collector distance, PVDF-HFP solution concentration, and the syringe pump's feeding rate) as the x-axes and the pore size and the membrane thickness ad the y-axes, as shown in **Figure 41**. The screening study shows that the voltage supply and the solution feeding rate are the top 2 influential factors/parameters among all the parameters studied. In comparison, changing the needle distance or the solution concentration have less effect on the morphology of the electrospun membrane.

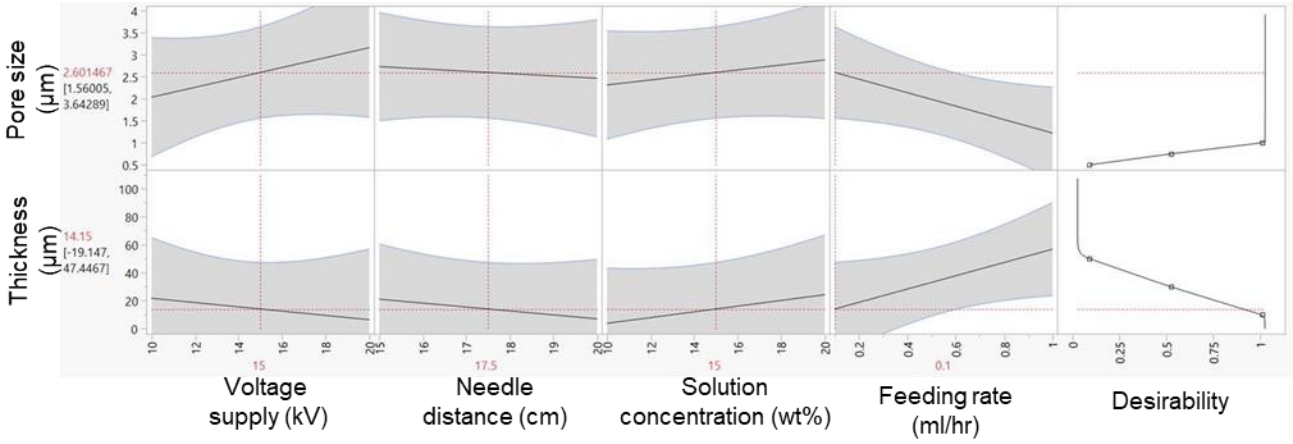

Figure 41. Results obtained from the screening study: effects of voltage supply, needle-collector distance, solution concentration, and solution feeding rate on the membrane morphology (i.e., pore size and thickness)

Interestingly, with increasing voltage supply or decreasing feeding rate, membrane pore size would increase, and membrane thickness would decrease, which is ideal for the properties of the membrane layer on a capillary-driven condenser. We are working on a fully factorial study to investigate the effect of the voltage supply and the solution feeding rate on the morphology of the electrospun membrane and looking for an optimized recipe of the membrane fabrication to achieve efficient heat and mass transfer through the membrane layer on a capillary-driven condenser.

Fabrication of Porous Metal Wick in a Scalable Way

As we mentioned earlier, porous metal wick can be fabricated in a scalable manner by electrodeposition. Our lab has developed a recipe to electrodeposit a single layer of inverse opal copper[23]. By using templating spheres with 10 μm diameter, we were able to fabricate a monolayer inverse opal copper with roughly 65% porosity, 5 μm thickness, and a model-predicted porosity of 5E-11m^2 permeability. The remaining challenge in the fabrication of inverse opal copper is sustaining a robust attachment and close to full coverage of the templating spheres during the electrodeposition step, which is critical to the scale of the surface area we are able to fabricate.

Sintering copper powders is another scalable way to fabricate porous copper. We have preliminarily tried sintering copper powders using three different powders: spherical powders with diameter < 10 μm, spherical powders with diameter < 50 μm, and dendritic powders with size < 45 μm. The resulting porous copper structures are shown in the SEM images in **Figure 42**.

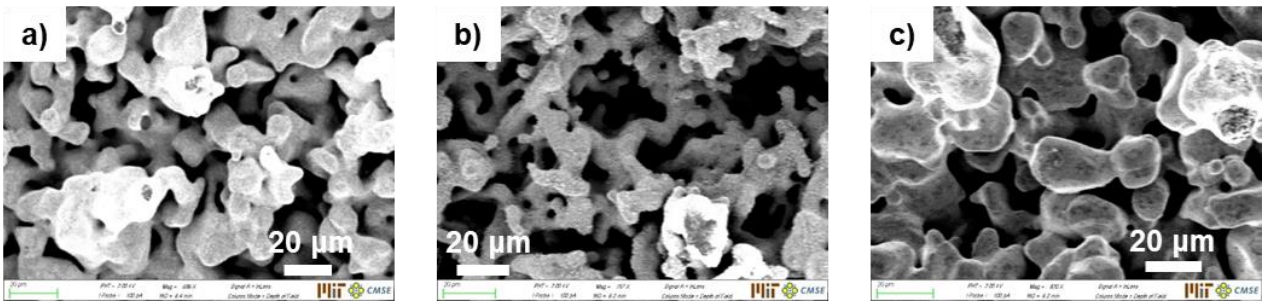

Figure 42. SEM images of sintered copper powders. (a) spherical powders with diameter < 10 μm. (b) spherical powders with diameter < 50 μm. (c) dendritic powders with size < 45 μm.

Due to the size of the tube furnace, we only fabricated sintered copper powder surfaces on the scale of 1 cm. However, sintering copper powers is a highly scalable technique as can be seen in the heat pipe industry. For the capillary-driven condenser, a small thickness (ideally under 200 μm) is required for the porous wick layer in order to reduce thermal resistance of the wick layer. Microporous copper wick monolayers have been achieved by sintering in the literature[24], although depositing a monolayer of copper powders over a large surface area is still challenging. Sintering copper powders with smaller size could keep the wick thickness small while depositing multiple layers of powders. However, the wick permeability would decrease with the size of the powders. The permeability of a sintered powder wick can be estimated by[25]:

$$\kappa = \frac{{d_{\text{powder}}}^2 {\phi_{\text{w}}}^2}{150(1-\phi_{\text{w}})^2} \quad (21)$$

where κ is the permeability of the sintered powder wick, d_{powder} is the size/diameter of the powders, and ϕ_{w} is the porosity of the sintered powder wick. Sintered copper powders has shown a porosity of ~50% in literature. We believe sintering copper powders with diameter of ~ 50 μm would be good to balance both the thickness and the permeability of the wick layer. Assuming a sintered copper wick made by four layers of 50 μm copper spheres with a porosity of 50%, we expect the copper wick's permeability to be ~1.7E-11m^2, which is comparable to the permeability of the copper foam we have been using for the proof of concept study.

Heat Transfer Prediction for Membrane-Covered Porous Copper Wick

We built a heat and mass transfer model for the electrospun-fiber covered porous copper based on vapor transport through the membrane pores and heat conduction through the condensate filled porous copper. **Figure 43** shows the model prediction for condensation heat transfer performance

of different capillary-driven condensers made of electrospun membrane covered porous copper. Three different porous copper were used as the wick layer in the model:

(a) Copper foam with 200 μm thickness, 65% porosity, and 1E-11 m^2 permeability.
(b) Inverse opal copper with 5 μm thickness, 65% porosity, and 5E-11 m^2 permeability.
(c) Sintered copper spheres with 200 μm thickness, 50% porosity, and 1.7E-11m^2 permeability.

(a) is what we have in lab and is commercially available. (b) is a structure that we are fabricating in lab. (c) is a common structure in heat pipe industries and we are considering fabricating. All three plots shown in **Figure 43** were obtained at a given vapor temperature (T_v = 35°C) and a subcool of 5°C. X-axis is pore size of the electrospun membrane and Y-axis is the corresponding heat flux predicted by the model. Red, blue, and green lines correspond to three different membrane porosity: 0.9, 0.8, and 0.7. Different thickness of lines means different membrane thickness. The black dash line denotes filmwise condensation predicted by the Nusselt model. In our model, heat flux would drop to zero when "flooding" occurs; this is not true in reality but is used as an indicator for "flooding" in the modelling results.

Figure 41(a) and **Figure 43**(c) are similar: with higher membrane pore size (increasing X-axis), higher porosity (red line), and smaller membrane thickness (10 μm thick denoted by the thinnest line), heat transfer gets much enhancement and no flooding occurs throughout the sweep. The similarity between these two plots is because we prescribed similar properties for the copper foam (corresponding to the **Figure 43**(a) and the sintered copper (corresponding to Figure 41(c)).

The lines in **Figure 43**(b) (corresponding to inverse opal copper) are not smooth due to the incremental sweep other than a continuous sweep we performed. Heat flux given by the same membrane increases faster in **Figure 43**(b) as compared to other two plots, but also induces flooding easier, which is because: the ultra-thin inverse opal (5 μm thick) could greatly reduce the thermal resistance of the water-filled porous copper but on the other hand, these thin structures are easier to flood (condenser liquid cannot be completely drained from the edge of the thin wick).

Overall, the model guided us to fabricate a membrane that is thin (on the order of 10 μm), highly porous (90%), and has a large pore size (on the order of 1 μm); we also wanted to make sure that flooding would not occur on this membrane under a sufficient subcool (at least 5°C). Once we complete the parametric optimization for electrospinning fibrous membranes, we will combine the optimized membrane with a porous structured copper substrate to make a scalable version of the

capillary-driven condenser. We expect to show over 5x enhancement on the electrospun membrane covered sintered copper powder without flooding under a subcool of 5°C, as predicted by model.

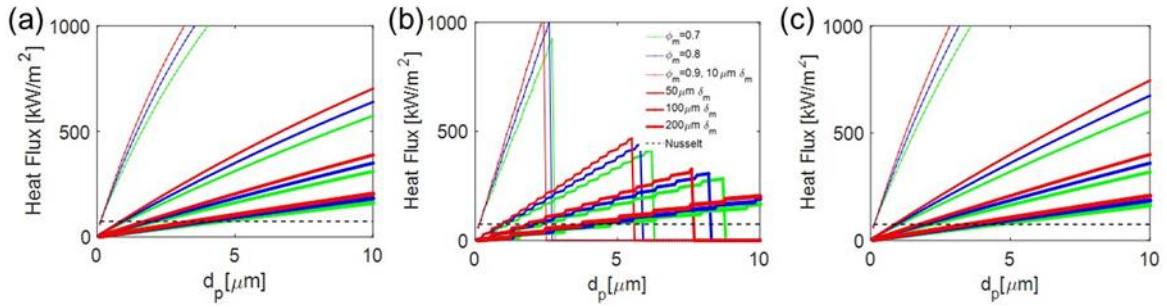

Figure 43. Condensation heat transfer performance of different types of porous copper covered by electrospun fibers, as predicted by heat and mass transfer model. (a) electrospun fibers in combination with a copper foam with 200 µm thickness, 65% porosity, and 1E-11 m^2 permeability. (b) electrospun fibers in combination with inverse opal copper with 5 µm thickness, 65% porosity, and 5E-11 m^2 permeability. (c) electrospun fibers in combination with sintered copper spheres with sphere diameter 50 µm, thickness 200 µm, 50% porosity, and 1.7E-11m^2 permeability.

REFERENCES

1. ICF-International, *Catalog of CHP Technologies*, in *Combined Heat and Power Partnership Program*, E.P.A. (EPA), U. S. Environmental Protection Agency (CHPPP): Washington, D.C.(2008).
2. Hao, M., Shi, J. & Maulbetsch, J. New Concepts of Water Conservation Cooling and Water Treatment Technologies. in *Program on Technology Innovation* (Electric Power Research Institute (EPRI), 2012).
3. Wilhelm, N. The surface condensation of steam. *Z. Ver. Dtsch. Ing.* 569–575 (1916).
4. Das, A. K., Kilty, H. P., Marto, P. J., Andeen, G. B. & Kumar, A. The Use of an Organic Self-Assembled Monolayer Coating to Promote Dropwise Condensation of Steam on Horizontal Tubes. *J. Heat Transfer* **122**, 278 (2002).
5. Marto, P. J. & Wanniarachchi, A. S. Evaluation of organic coatings for the promotion of dropwise condensation of steam. **29**, 1109–1117 (1986).
6. Vemuri, S. & Kim, K. J. An experimental and theoretical study on the concept of dropwise condensation. *Int. J. Heat Mass Transf.* **49**, 649–657 (2006).
7. Vemuri, S., Kim, K. J., Wood, B. D., Govindaraju, S. & Bell, T. W. Long term testing for dropwise condensation using self-assembled monolayer coatings of n-octadecyl mercaptan. *Appl. Therm. Eng.* **26**, 421–429 (2006).
8. Rose, J. W. Dropwise condensation theory and experiment: A review. *Proc. Inst. Mech. Eng. Part A J. Power Energy* **216**, 115–128 (2002).
9. Enright, R., Nenad Miljkovic, Alvarado, J. L., Kim, K. & Rose, J. W. Dropwise Condensation on Micro- and Nanostructured Surfaces. *Nanoscale Microscale Thermophys. Eng.* **18**, 223–250 (2014).
10. Schmidt, E., Schurig, W. & Sellschopp, W. Condensation of water vapour in film and drop form. *Z Ver Dtsch Ing* **74**, 544–544 (1930).
11. Byon, C. & Kim, S. J. The effect of meniscus on the permeability of micro-post arrays. *J. Micromechanics Microengineering* **21**, (2011).

12. Berman, A. S. Free molecule transmission probabilities. *J. Appl. Phys.* (1965). doi:10.1063/1.1702984

13. Rose, J. W. Some aspects of condensation heat transfer theory. *Int. Commun. Heat Mass Transf.* **15**, 449–473 (1988).

14. Tsuchiya, T., Inoue, A. & Sakata, J. Tensile testing of insulating thin films; Humidity effect on tensile strength of SiO2 films. *Sensors Actuators, A Phys.* **82**, 286–290 (2000).

15. Yoshioka, T., Ando, T., Shikida, M. & Sato, K. Tensile testing of SiO2 and Si3N4 films carried out on a silicon chip. *Sensors Actuators, A Phys.* **82**, 291–296 (2000).

16. Tang, H. *et al.* Review of applications and developments of ultra-thin micro heat pipes for electronic cooling. *Appl. Energy* **223**, 383–400 (2018).

17. Kim, J., Kim, R. & Kwon, H. Preparation of copper foam with 3-dimensionally interconnected spherical pore network by electrodeposition. *Electrochem. commun.* **10**, 1148–1151 (2008).

18. Preston, D. J. *et al.* Gravitationally-Driven Wicking for Enhanced Condensation Heat Transfer. (2018). doi:10.1021/acs.langmuir.7b04203

19. Varanasi, K. K., Hsu, M., Bhate, N., Yang, W. & Deng, T. Spatial control in the heterogeneous nucleation of water. **094101**, 1–4 (2010).

20. Reay, D. A., Kew, R. J. & McGlen, R. J. Chapter 3 - Heat pipe components and materials. in *Heat Pipes (Sixth Edition)* 65–94 (Butterworth Heinemann, 2014).

21. Ahmed, F. E., Lalia, B. S. & Hashaikeh, R. A review on electrospinning for membrane fabrication : Challenges and applications. *DES* **356**, 15–30 (2015).

22. T. Berling & Runeson, P. Efficient evaluation of multifactor dependent system performance using fractional factorial design. *IEEE Trans. Softw. Eng.* 769–781 (2003).

23. Carlos, D. D., Shetty, R. M., Cheung, S., Gopinath, A. & Wang, E. N. Rational Fabrication of Nano-to-Microsphere Polycrystalline Opals Using Slope Self-Assembly. (2021). doi:10.1021/acs.langmuir.1c01857

24. Hoenig, S. H. & Iii, R. W. B. Dropwise Condensation on Superhydrophobic Microporous Wick Structures. **140**, 1–7 (2018).

25. Leong, K. C., Liu, C. Y., Avenue, N. & Lu, G. Q. Characterization of Sintered Copper Wicks Used in Heat Pipes. **308**, 303–308 (1997).